

Structure and Dynamics of Aqueous Dispersions of Highly-Branched Monodisperse Phytoglycogen Nanoparticles

by

John Atkinson

A Thesis

Presented to

The University of Guelph

In partial fulfillment of the requirements
for the degree of
Master of Science
in
Biophysics

Guelph, Ontario, Canada

© John Atkinson, August, 2015

Abstract

Structure and Dynamics of Aqueous Dispersions of Highly-Branched Monodisperse Phytoglycogen Nanoparticles

John Atkinson
University of Guelph, 2015

Advisor:
John Dutcher

Phytoglycogen is a natural monodisperse polysaccharide nanoparticle isolated from sweet corn.

The particles are highly hydrophilic resulting in high water retention, low viscosity, and extraordinary stability in water. We use neutron scattering to study the structure and dynamics of aqueous dispersions of phytoglycogen. Small angle neutron scattering (SANS) showed that the particles have uniform density with radius 17.4 ± 1.6 nm, and allowed the determination of the concentration dependence of the inter-particle spacing, and the hydration number ($n_H = 22.5 \pm 2.5$ nm per glucose monomer). Quasielastic neutron scattering showed sub-diffusive motion of the hydration water and provided an independent value of the hydration number ($n_H = 25.8 \pm 4.6$ nm per glucose monomer), in agreement with the SANS result. Taken together, the results show that between 250-285% of the hydrated particle mass is due to hydration water.

Acknowledgments

I would like to thank my advisor Dr. John Dutcher for his help, support, patience and guidance over the past few years. I would also like to thank him for the opportunity to travel to Oak Ridge National Laboratory (ORNL) to perform my experiments and experience science performed at sophisticated facilities. Also thanks to Mirexus Biotechnologies Inc. for the samples and previous knowledge required to perform this research.

Thanks to my advisory committee: Dr. Mario Monterio, Dr. Stefan Kycia, and Dr. Vladimir Ladizhansky for their guidance and discussions during our meetings. Same thanks extends to Dr. Robert Wickham for his helpful discussions during group meetings.

I would also like to thank Dr. John Katsaras and Dr. Jonathan Nickels at ORNL for their collaboration and expertise at performing the neutron scattering experiments. A special thanks to Dr. Nickels for without his knowledge and aid I would still be trying to stitch the data together.

Thanks to Jay Leitch for helpful conversations and the use of his lab to examine phytoglycogen. Also thanks to my officemates, Erin Shelton, Richard Parg, Josh Mogyoros, and Ben Baylis for brainstorming and discussions on sometimes random topics. Special thanks to past post-doctoral fellows Maximilliano Giuliani and Adam Raegen for their useful discussions and lab guidance to help me become a better scientist.

Table of Contents

Introduction and Background	1
1.1 Phyloglycogen	1
1.1.1 Interactions of Phyloglycogen With Water	2
1.1.2 Applications of Phyloglycogen	3
1.2 Dendrimers	4
1.2.1 Self-Limited Growth of Dendrimers	5
1.2.2 Radial Density Profile of Dendrimers	6
1.4 Neutron Scattering.....	8
1.4.1 Small Angle Neutron Scattering.....	9
1.4.2 Quasielastic Neutron Scattering	10
1.5 Scope of Thesis	10
Scattering Theory.....	12
2.1 Introduction to Scattering.....	12
2.2 Neutron Scattering.....	13
2.3 Neutron Elastic Scattering Theory	13
2.4 Scattering from Individual Atoms.....	14
2.5 Scattering from a Macromolecule	18
2.6 Scattering from a Dense Collection of Macromolecules or Particles	20

2.7 Contrast Matching	21
2.8 Small Angle Neutron Scattering	24
2.8.1 Form Factor	25
2.8.2 Structure Factor	26
2.9 Quasielastic scattering.....	28
Materials, Methods and Analysis.....	31
3.1 Sample Preparation	31
3.1.1 Purification	31
3.1.2 Bradford Assay for Determining Protein Concentration.....	34
3.2 Dynamic Light Scattering	35
3.3 Neutron Scattering.....	37
Results and Discussion	40
4.1 Bradford Assay.....	40
4.2 Dynamic Light Scattering	41
4.3 Neutron Scattering.....	42
4.3.1 SANS Structure, Spacing, Hydration Water and Molecular Weight	42
4.3.2 Elastic and Quasielastic Dynamics.....	47
Summary and Future Work.....	58
5.1 Summary of Results	58
5.2 Future Work	59

5.2.1 Light Scattering	59
5.2.2 High Resolution Imaging of Phytoglycogen Nanoparticles	60
5.2.3 Further Neutron Scattering Experiments	60
References	61

List of Figures

Figure 1: Chain and branch structure of phytoglycogen nanoparticles . -----	1
Figure 2: Relative viscosity of phytoglycogen as a function of phytoglycogen concentration.----	2
Figure 3: Relative water retention of phytoglycogen -----	4
Figure 4: Snapshot of a ninth generation dendrimer -----	7
Figure 5: Schematic representation of the elastic scattering -----	9
Figure 6: Schematic showing the geometry for scattering of radiation from an isolated particle.	15
Figure 7: Dependence of scattering length as a function of fraction of deuteration -----	22
Figure 8: Contrast matching applied to a core-shell particle-----	23
Figure 9: Generic spectrum of a backscattering experiment -----	29
Figure 10: Nominal pore sizes for specific molecular weight cut offs -----	32
Figure 11: Schematic diagram of the phytoglycogen ultrafiltration procedure -----	33
Figure 12: Brookhaven Dynamic Light Scattering Spectrometer -----	37
Figure 13: Calibration curve for the Bradford protein assay-----	41
Figure 14: Autocorrelation function for a dispersion of ultra-filtered phytoglycogen -----	42
Figure 15: SANS results of phytoglycogen dispersions. -----	44
Figure 16: Neutron contrast series used to establish the SLD of phytoglycogen -----	45
Figure 17: Fixed window elastic scattering data-----	49
Figure 18 QENS data for phytoglycogen dispersions-----	50
Figure 19. Fitting of QENS data.-----	52
Figure 20 Fitting of QENS data. Normalized area terms a_i -----	53

Figure 21 Fitting of FWHM values for bulk and hydration water translation in phytoglycogen

dispersions.-----56

Chapter 1

Introduction and Background

1.1 Phytoglycogen

Phytoglycogen is a highly branched polysaccharide produced in the form of monodisperse nanoparticles by isoamylase deficient plants. The inhibition of debranching during the synthesis of amylopectin results in a dense polymer similar to that of glycogen¹. Both types of these molecules consist of glucose monomers that form chains via α -(1→4) glycosidic linkages and are regularly branched via α -(1→6) linkages^{1–3}(Figure 1). Phytoglycogen and glycogen are chemically identical but vary in terms of chain length and the rate of branching due to the difference in the enzymes used during synthesis. This repeating cycle of chain growth and branching is similar to that for synthetic dendrimers (discussed in 1.2).

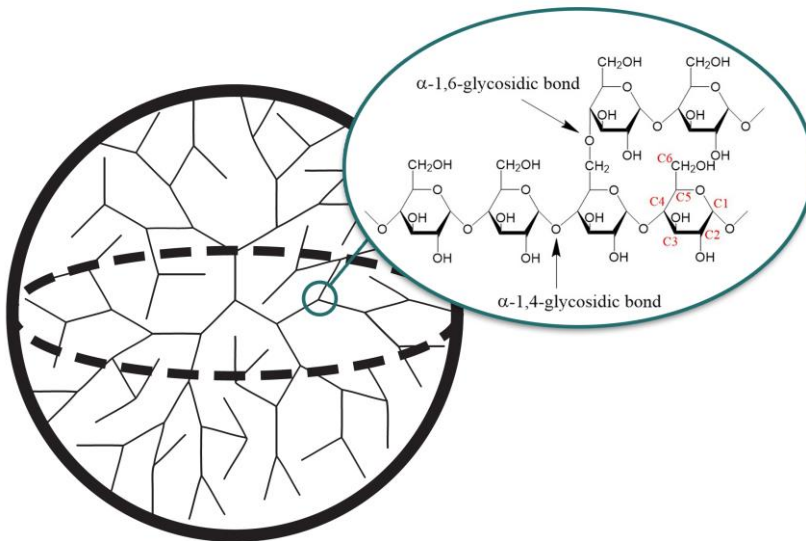


Figure 1: Chain and branch structure of phytoglycogen nanoparticles using glucose monomers.

Glycogen has been extensively studied and its basic structure^{4–8}, enzymes^{9–11}, and evolutionary significance are well understood¹². Phytoglycogen has not so been extensively studied, with recent experiments focusing on enzymatic and chemical modification¹³.

1.1.1 Interactions of Phytoglycogen With Water

Because of the hydrophilic nature of the glucose subunits and its highly branched structure, phytoglycogen has unique interactions with water. Rheology studies show that phytoglycogen is highly soluble, reaching very concentrated solutions, ~25% w/w, before a divergence in viscosity is observed¹⁴ (Figure 2). Gravimetric analysis has shown that dry phytoglycogen absorbs 28% of its mass in water after long periods of time (several days) under high relative humidity conditions (RH =100%)¹⁵. This large absorption of water is expected, given the large number of available hydroxyl groups.

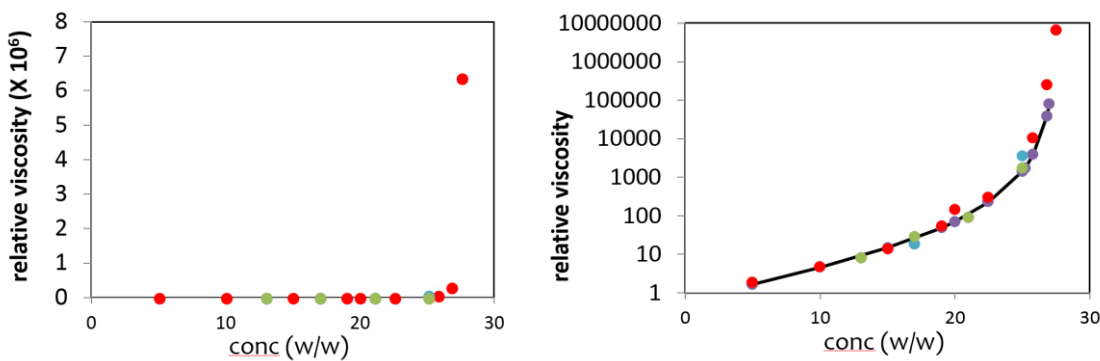


Figure 2 Relative viscosity of phytoglycogen (zero shear viscosity relative to that of water) as a function of phytoglycogen concentration. A sharp divergence in viscosity can be seen at concentrations close to 25% w/w. The same data is shown in both plots, with a linear scale used in the left plot and a logarithmic scale used in the right plot. The different colour data points correspond to different salt concentrations showing that electrostatics are not important. Data from Erszsi Papp-Szabo¹⁴.

1.1.2 Applications of Phytoglycogen

The unique properties of phytoglycogen nanoparticles make them desirable as functional ingredients for a broad range of personal care, nutraceutical and biomedical applications.

Mirexus Biotechnologies Inc., a start-up company from our academic laboratory, is commercializing the monodisperse phytoglycogen nanoparticle technology in these areas of application (Mirexus has supplied the phytoglycogen nanoparticles used in the present study).

The ability of phytoglycogen nanoparticles to absorb and slowly release water makes them an attractive moisturizing agent in cosmetics formulations. In fact, phytoglycogen outperforms the leading high-end commercial moisturizing agent, hyaluronic acid, in terms of water retention over long periods of time (Figure 3). Although phytoglycogen does not hydrate as extensively as hyaluronic acid, it has a slower time-release profile that makes it desirable as a long-term moisturizer¹⁴. The nanoparticles are also attractive for endurance sports drinks, providing a slow release of sugar to the athletes as they exercise. Phytoglycogen nanoparticles are perhaps most appealing for biomedical applications, e.g. as a drug delivery vehicle. The natural, biodegradable nature of phytoglycogen and the possibility of attaching drug and targeting molecules on the outer surface of the nanoparticles using carbohydrate chemistry techniques give it a significant advantage over other drug delivery vehicles, e.g. synthetic dendrimers, which have strong structural similarities to phytoglycogen^{2,9,16,17}.

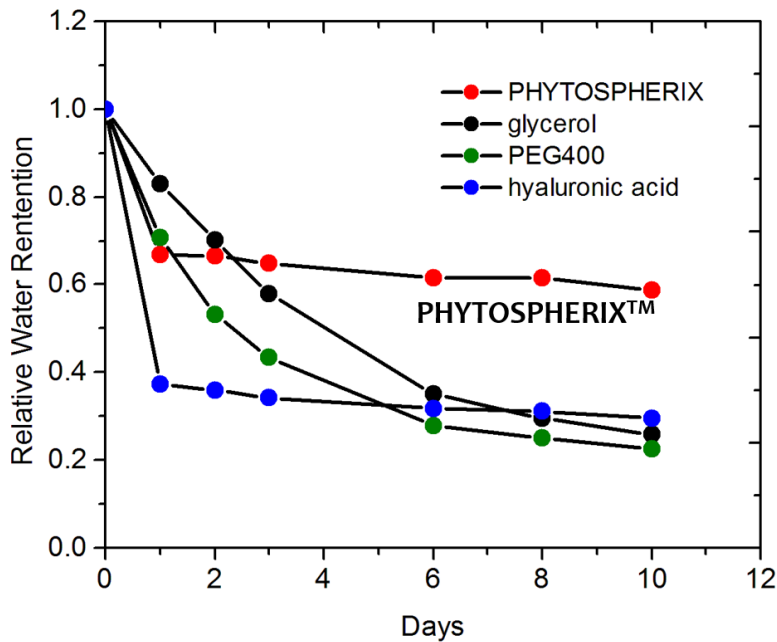


Figure 3 Relative water retention, measured gravimetrically, of phytoglycogen (Phytospherix) and other moisturizing agents used in cosmetics formulations. Phytoglycogen retains significantly more water at longer times in a dessicated environment.¹⁴

1.2 Dendrimers

It is useful to discuss the synthesis and structure of synthetic dendrimer molecules because of the similarities with the growth of natural dendrimers such as glycogen and phytoglycogen^{16,17}. The chemical synthesis of a dendrimer requires an iterative process, with each iteration producing the next generation of the dendrimer. Starting at a trifunctional core, known as generation zero (G0), chains are added to each of the functional sites, forming the first generation (G1). Each chain in G1 has two functional sites that serve as branching points for two linear chains that correspond to the second generation (G2) of the dendrimer¹⁸. This growth process continues until it is artificially terminated or until the density of the chains is large enough that the addition of more chains is sterically blocked as there is no accessible volume for new monomers to occupy. This

method of growth leads naturally to a maximum and uniform particle size, and is referred to as self-limited growth.

1.2.1 Self-Limited Growth of Dendrimers

We consider the dendrimer molecules to be characterized by functionality f and p monomers in each linear chain of length b between branching points: in G0, there is 1 monomer; in G1, there are fp monomers; in G2, there are $fp(f - 1)$ monomers; in G3, there are $fp(f - 1)^2$, ... The total number of monomers N_g in the dendrimer molecule can be written as a sum:

$$\begin{aligned} N_g &= 1 + fp + fp(f - 1) + fp(f - 1)^2 + \cdots fp(f - 1)^{g-1} \\ N_g &= 1 + fp[1 + (f - 1) + (f - 1)^2 + \cdots (f - 1)^{g-1}] \\ N_g &= 1 + fp \left[\frac{(f - 1)^g - 1}{f - 2} \right] \end{aligned}$$

Equation 1

Equation 1 corresponds to exponential growth in the number of monomers with increasing generation number g . Equation 1 can also be used to obtain an expression for the maximum generation for a dendrimer molecule from a consideration of packing constraints¹⁹. The volume occupied by a dendrimer molecule can be written as $v N_g$, where v is the volume of the monomer. The maximum accessible volume, corresponding to fully stretched chains, is $(4/3)\pi g^3 b^3$. Since the occupied volume cannot exceed the maximum accessible volume, this leads to an expression for the maximum generation g_{max} of a dendrimer:

$$g_{max} \approx -\frac{\ln\left(\frac{vfp}{(f-2)b^3}\right)}{\ln(f-1)}$$

Equation 2

This self-limiting growth process leads to monodispersity in the size of the dendrimer molecules.

1.2.2 Radial Density Profile of Dendrimers

Given the exponential growth of the number of monomers with generation, it was originally thought that the density of monomers increased exponentially with radial distance within the molecule, leading to a “hollow core – dense shell” picture. This picture was demonstrated mathematically by de Gennes and Hervet²⁰ and brought great excitement to the field of dendrimer research, because of the possibility of using the “hollow core” particles as a vehicle to deliver drugs. However, because they assumed a priori that subsequent generations occurred at larger radial distances, this necessarily produced a hollow core radial profile. Subsequent computer simulations and calculations showed that this was not necessarily true because of the flexibility of the chains within the molecule¹⁸. Computer simulations^{18,21,22}, refinements of self-consistent field theory calculations^{19,23}, together with small angle neutron scattering (SANS) experiments^{24,25} on high generation dendrimer molecules, have shown that growth at higher generations involves the folding back of the flexible chains into the center of the molecule, resulting in high molecular weight, monodisperse molecules that have a highly-branched outer surface and a dense core.

Back folding of the chains into the centre of the molecule at high generations was observed in Monte Carlo simulations performed by Goddard²⁶ and Likos & I.O Götze²⁷ in which they simulated polyamidoamine (PAMAM) dendrimers with generations 1 to 11 and tracked the location of monomers in each generation. Likos¹⁸ has provided a colour-coded pictorial representation of the distribution of monomers of different generations (Figure 4). This shows clearly that the monomers of the highest generation are uniformly distributed throughout the molecule.

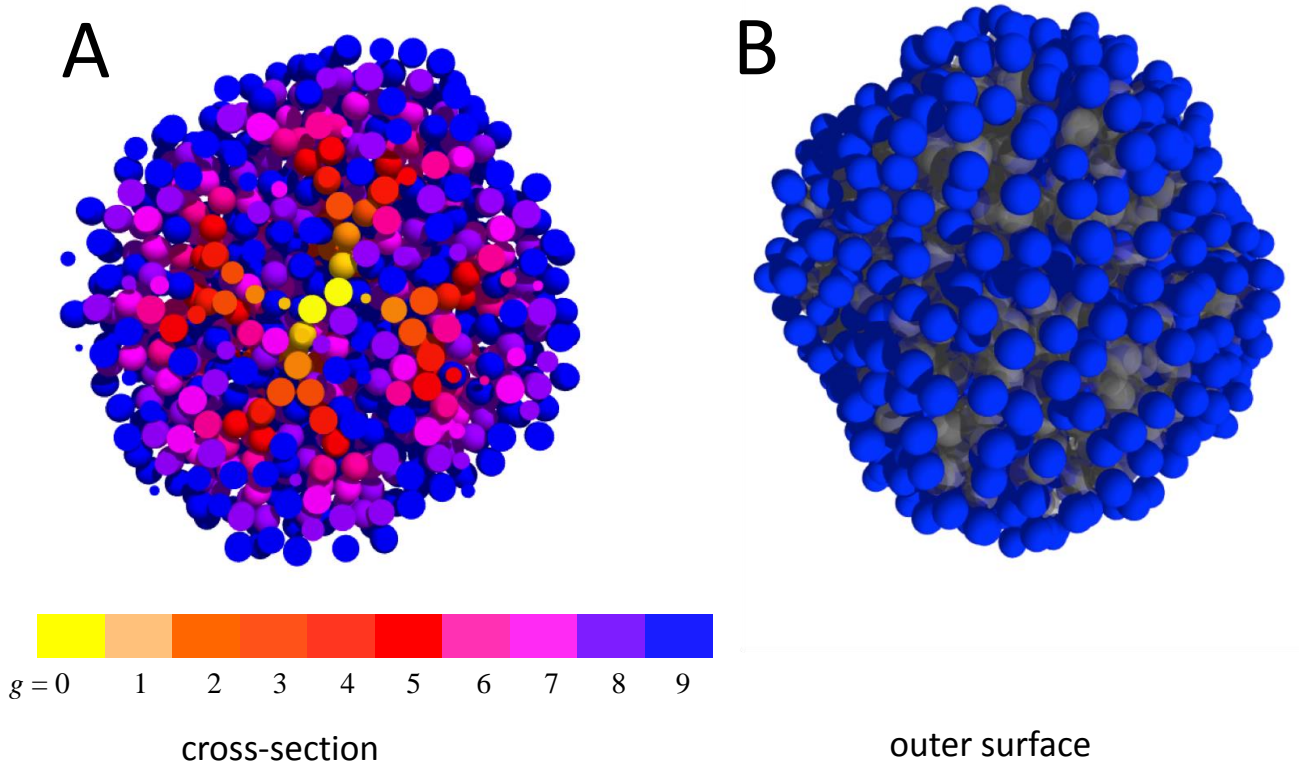


Figure 4 Simulated images of a ninth generation dendrimer. A) Cross-section though the centre of the dendrimer, revealing that higher order generation monomers are distributed uniformly throughout the volume of the dendrimer. B) Terminal groups (blue) decorate the surface of the dendrimer. Adapted from Likos¹⁸.

1.4 Neutron Scattering

Neutron scattering is an ideal technique to study the interaction between a material and water. This is because neutron scattering yields very different results for hydrogen and its heavier isotope deuterium²⁸. Unlike x-ray scattering and light scattering, which scatter from the electron cloud of an atom or a difference in index of refraction between a particle and the surrounding medium respectively, neutrons scatter directly from the nucleus. Because the nucleus is significantly smaller than the electron cloud probed in x-ray scattering, the scattering efficiency is very low and long data collection times are necessary to achieve sufficient statistics. This is in addition to the collection times due to the significant reduction in flux of neutron sources compared to x-ray sources. It is possible to use this low scattering efficiency to our advantage to study highly concentrated aqueous dispersions with little risk of secondary scattering, which would complicate the analysis²⁹.

A scattering event can be characterized by the change in momentum of the incident radiation. The incident neutrons of wavelength λ have momentum $hk = 2\pi h/\lambda$ and the scattered neutrons have momentum hk' . This change in momentum is called the momentum transfer $hq = h|k - k'| = \frac{4\pi h}{\lambda} \sin\theta$, as illustrated in Figure 5. Bragg's law for elastic scattering from a periodic lattice states that constructive interference, i.e. large scattering intensity, is obtained when $\lambda = 2d \sin\theta$, where d is the lattice spacing. By combining Bragg's law with the momentum transfer $hq = \frac{4\pi h}{\lambda} \sin\theta = \frac{2\pi h}{d}$, we can see that large (small) q values probe small (large) length scales d . The theory of neutron scattering is explained in more detail in chapter 2.

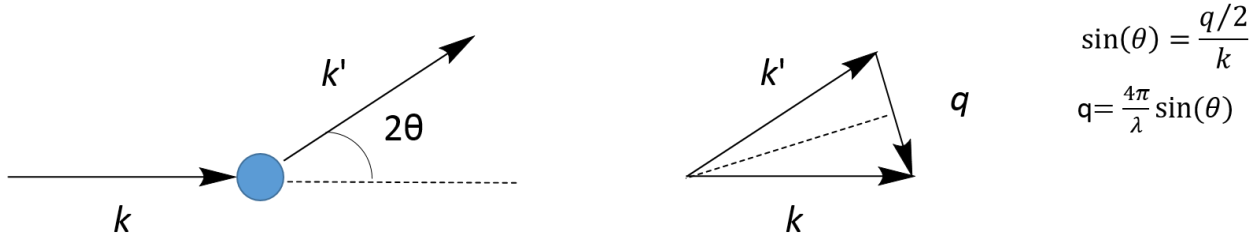


Figure 5: Schematic representation of the elastic scattering of radiation. The incident radiation has wavevector k and the scattered radiation has wavevector k' . The momentum transfer is given by hq .

1.4.1 Small Angle Neutron Scattering

Cold neutrons have a very small wavelength ($\sim 10^{-10}$ m) and by measuring scattering at small angles (typically $\sim 0.01 - 10^\circ$), a large range of length scales can be probed (~ 1 to 100 nm). This is referred to as small angle neutron scattering (SANS), and it is ideal for structural investigations of nanomaterials. If the system corresponds to a dispersion of particles in an incompressible solvent, the scattering intensity can be written as³⁰

$$I(q) = \varphi V_p \Delta\rho^2 P(q) S(q)$$

Equation 3

where φ is the volume fraction of the particles, V_p is the volume per particle, $\Delta\rho$ is the difference (contrast) between the scattering length density of the particles and the solvent, $P(q)$ is the form factor of the particles and $S(q)$ is the corresponding structure factor. The first three terms on the right hand side of Equation 3 are constant and simply introduce a scaling factor. The form factor

$P(q)$ is the intra-particle interference contribution, providing information about the particle shape and internal structure. The structure factor $S(q)$ is the inter-particle interference contribution, providing information on the inter-particle spacing and interactions between particles.

At low concentrations, the particle spacing is so large that they can be assumed to be non-interacting. In this limit, $S(q) \rightarrow 1$ and the form factor $P(q)$ can be determined. $P(q)$ can then be used to determine the structure factor $S(q)$ at larger particle concentrations.

1.4.2 Quasielastic Neutron Scattering

If energy is gained or lost during the scattering event, the scattering process is referred to as inelastic, with energy transfer ϵ and momentum transfer hq . The energy transfer ϵ characterizes fluctuations in the particle spacing, i.e. diffusion of particles, by measuring the change in energy of the neutron based on the energy gained or lost from the particle's motion. This makes it possible to study dynamical processes using neutron scattering and this will be discussed in detail in Chapter 2.

1.5 Scope of Thesis

The purpose of this thesis is to characterize dispersions of monodisperse, hyperbranched phytoglycogen polysaccharide nanoparticles to determine their density profile, particle size, inter-particle interactions, and their degree of hydration. These measurements were performed using two neutron scattering techniques: small angle neutron scattering (SANS) and quasi-elastic neutron scattering (QENS).

In Chapter Two, I describe the theory of neutron scattering for the experiments described in this thesis. In Chapter Three, I describe the experimental procedures and the data analysis techniques. In Chapter Four, I present and discuss the results of the neutron scattering experiments. In Chapter Five, I provide a summary of the results and suggest future experiments and analysis.

Chapter 2

Scattering Theory

2.1 Introduction to Scattering

Scattering of radiation, in particular small angle scattering, is widely used to characterize biological soft matter systems. Scattering experiments complement microscopy techniques, providing information on the bulk properties of the materials instead of being restricted to the surface properties. Given that small angle scattering is sensitive to length scales ranging from 1-100 nm, it is an invaluable technique for studying the domain of colloidal nanoparticles²⁹.

Light, X-rays, and neutrons are commonly used in scattering experiments. Although the details of the scattering are different (variations in index of refraction for light, variations in electron densities for x-rays, and variations in nuclear density for neutrons), they all share the same scattering theory framework.

As discussed in Chapter 1, the Bragg model can be used to understand the length scales that can be probed with radiation of wavelength λ for a periodic lattice. This model is too simple to describe most soft matter systems because the samples in general are not crystalline and the constituent atoms diffuse, but it is still useful in learning about the length scales probed in the scattering experiment. In these experiments, the scattering intensity is typically plotted as a function of wavevector transfer q , which is the difference in wavevector between the incident and scattered waves.

2.2 Neutron Scattering

Neutrons are non-destructive probes which are ideal for studying biological soft matter, which is easily damaged by high energy X-rays. Since neutrons scatter only from the nucleus of atoms, they have a large penetration depth since the scattering efficiency is small²⁹. The large penetration depth allows for the study of thick biological films or highly concentrated dispersions, which is not possible with other methods because of the presence of secondary scattering that greatly complicates the analysis of the data.

Another big advantage of neutrons is isotopic sensitivity: different isotopes can have significantly different scattering. One dramatic example of this is the high contrast between hydrogen (¹H) and deuterium (²H or D), for which scattered neutrons have opposite phases²⁸. This property is extremely useful when scattering from aqueous suspensions of biological macromolecules, which are typically rich in hydrogen and can be very easily distinguished from a D₂O solvent.

2.3 Neutron Elastic Scattering Theory

In a neutron scattering experiment, the intensity of the scattering is measured as a function of the wavevector transfer q and the energy transfer ϵ . In elastic scattering, $\epsilon = 0$, the scattering is described by $I(q)$, and structural information is obtained. Nonzero energy transfer, corresponding to quasielastic and inelastic scattering, describes the dynamics of the sample (see Section 2.9).

2.4 Scattering from Individual Atoms

The interaction between the incident neutrons and the nucleus is due to the strong nuclear force for non-magnetic systems²⁹. For magnetic systems, one would also have to account for the spin S of the incident neutrons ($S = 1/2$). Given that the effective range of the strong nuclear force is $\sim 10^{-15}$ m and that λ is on the order of 10^{-10} m, the internal structure of the nucleus cannot be resolved and it can be treated as a point scatterer^{25,29}.

The incident neutron beam can be represented by a plane wave

$$\Psi_i = e^{ik \cdot r}$$

Equation 4

where k is the incident neutron wavevector. The scattered wave has spherical symmetry due to isotropic scattering from the point scatterer, with wavevector k' and an amplitude that decreases as $1/r$:

$$\Psi_{sc} = -\frac{b}{r} e^{ik' \cdot r}$$

Equation 5

The scattering geometry is illustrated in Figure 6

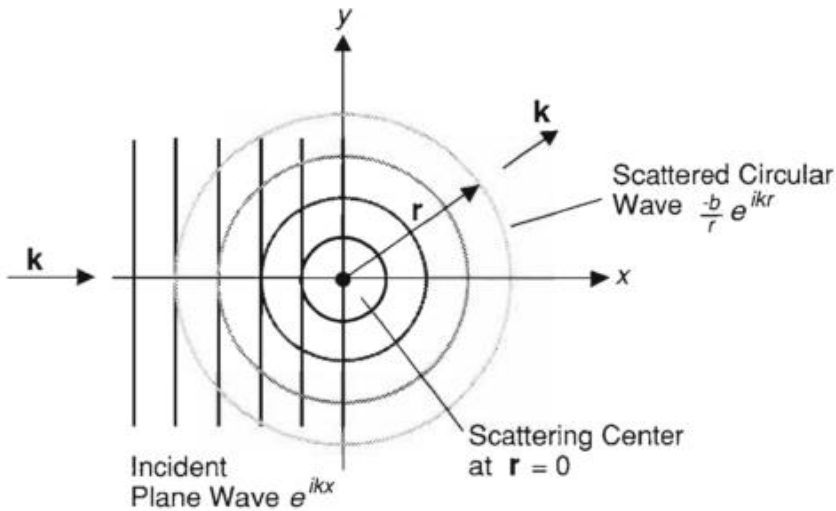


Figure 6 Schematic showing the geometry for scattering of radiation from an isolated particle.

The complex variable b is known as the scattering length, which has units of length²⁸ and is a measure of the probability of scattering from the nucleus (probability of bb^*). The scattering length can be negative which indicates scattering of the opposite phase. The scattering length for each element is independent of the atomic number Z and therefore varies “randomly” across the periodic table³¹. There is no theory for its calculation; all scattering lengths are experimentally measured and tabulated²⁸.

To measure the intensity, one needs to know how many neutrons are scattered into a specific direction. When the sample-to-detector distance is large, it is possible to define a solid angle $d\Omega$ to represent the detector. It is then possible to define the differential scattering cross section $d\sigma_s/d\Omega$, which is the probability of a neutron being scattered into the solid angle $d\Omega$. We can write

$$\frac{d\sigma_s}{d\Omega} = \frac{\text{Neutrons per unit time scattered into } d\Omega}{\text{Number of incident neutrons per area per second}}$$

Equation 6

Integrating over all solid angles, we obtain the total scattering cross-sectional area:

$$\sigma_s = 4\pi b^2$$

Equation 7

The total scattering cross-sectional area is the “effective area” that the nucleus presents to the incident neutrons.

To obtain the scattering intensity, we can write Equation 6 as:

$$\frac{d\sigma_s}{d\Omega} = \frac{1}{\Phi} \frac{1}{d\Omega} \sum W$$

Equation 8

where Φ is the neutron flux and W is the number of transitions (scattering events) per second.

By using Fermi’s Golden rule, a box normalization and a Fermi pseudopotential, Van Hove showed that the scattering intensity for the system could be written as³²:

$$I(q, \epsilon) = \frac{1}{h} \frac{k'}{k} \sum_{j,k} b_j b_k \int_{-\infty}^{\infty} \langle e^{-iq \cdot r_k(0)} e^{iq \cdot r_j(t)} \rangle e^{-i\epsilon t} dt$$

Equation 9

In Equation 9, the scattering intensity is a function of both scattering wavevector and energy transfer.

Because the scattering length value for an isotope depends on its spin state, it is necessary to calculate the averages of b and b^2 for different spin states (\bar{b} and $\bar{b^2}$). If a spin state b_i occurs with frequency f_i , then we can define \bar{b} and $\bar{b^2}$ as

$$\bar{b} = \sum_i f_i b_i$$

$$\bar{b^2} = \sum_i f_i b_i^2$$

This allows us to write the double summation in Equation 9 as

$$\sum_{j,k} \bar{b_j} \bar{b_k} A_{jk} = \sum_{j \neq k} (\bar{b})^2 A_{jk} + \sum_j (\bar{b^2} - (\bar{b})^2) A_{jj}$$

Equation 10

where A_{jk} is the integral. The first term on the right hand side of Equation 10 is known as the coherent scattering term and we define $b_{coh} = \bar{b}$. The second summation on the right hand side of Equation 10 corresponds to incoherent scattering, with $b_{inc} = \sqrt{\bar{b}^2 - (\bar{b})^2}$. Coherent scattering provides structural information as it accounts for scattering between atoms and it is sensitive to q as it is sensitive to the space between atoms. Incoherent scattering is insensitive to length scales and therefore q and can be used to determine dynamics in the sample as it corresponds to scattering from the same atom ($j = k$) at different times²⁹.

2.5 Scattering from a Macromolecule

Equation 9 describes the scattering from an individual atom and pairs of atoms and can be expanded to describe scattering from larger macromolecules at smaller q values. To do this, one can sum the individual scattering events from each macromolecule yielding

$$A(q) = \sum_{all\ atoms} b(r) e^{iq \cdot r}$$

Equation 11

where $A(q)$ is the scattering amplitude of the sample and $b(r)$ is the scattering length of an atom at distance r from the origin. When considering macromolecules, it is useful to convert the summation in Equation 11 to an integral over the volume of the macromolecule. To do this, the

discrete scattering length densities need to be converted to a continuous function known as the scattering length density $\rho(r)$, which represents the scattering length per unit area:

$$\rho(r) = \frac{1}{V} \sum_i^N b_i$$

Equation 12

where V is the volume occupied by the constituent atoms. Therefore Equation 11 can be rewritten as:

$$A(q) = \int \rho(r) e^{iq \cdot r} d^3r$$

Equation 13

The corresponding scattering intensity is given by:

$$I(q) = A * A^* = \iint \rho(r_1) \rho(r_2) e^{iq \cdot (r_1 - r_2)} d^3r_1 d^3r_2$$

Equation 14

Since the double integral only depends on the distance between r_1 and r_2 , it is possible to integrate over all the differences in length to get

$$I(Q) = \frac{1}{V} \int \Delta\rho^2 e^{iQ\cdot r} d^3 r$$

Equation 15

where $\Delta\rho$ is the difference in scattering length densities between the sample and solvent for single particle systems. For a macromolecule surrounded by solvent, $\Delta\rho$ is regarded as $\rho_{solvent} - \rho_{macromolecule}$.

2.6 Scattering from a Dense Collection of Macromolecules or Particles

We can extend the theory presented in the previous section to examine collections of macromolecules to evaluate of the particle-particle spacing in a dense collection of particles.

For a dense collection of particles at long length scales, we can no longer consider the scattering to be described by a continuous function because of the fluctuations in the scattering length density. By solving Equation 14, one can obtain a discrete version of Equation 15 corresponding to scattering on longer length scales. If all particles are identical, we can write³²:

$$I(q) = b_{coh}^2 \sum_{j,k} \langle e^{iq \cdot (r_j - r_k)} \rangle$$

Equation 16

where b_{coh} is the average scattering length of the particles and each term in the summation represents an ensemble averaging of all pairs of particles j and k .

2.7 Contrast Matching

For neutron scattering from aqueous dispersions of particles, there is an interesting possibility of matching the scattering length density of the solvent to that of the particles. Under this contrast matching condition, all or part of the particles will be matched to the solvent. In the simplest case of particles with uniform neutron scattering length density (NSLD), the contrast match condition reduces the scattering intensity to very low levels at a single match point. Neutron scattering from aqueous dispersions of particles is particularly amenable to contrast matching since one can exploit the large difference (including a difference in sign) in neutron scattering from H₂O and D₂O^{28,29,31,33}. Mixtures of H₂O and D₂O will have a scattering length density that is a linear combination of that of the two constituents, and the available range of values spans a wide range of biological macromolecules³³ (see Figure 7).

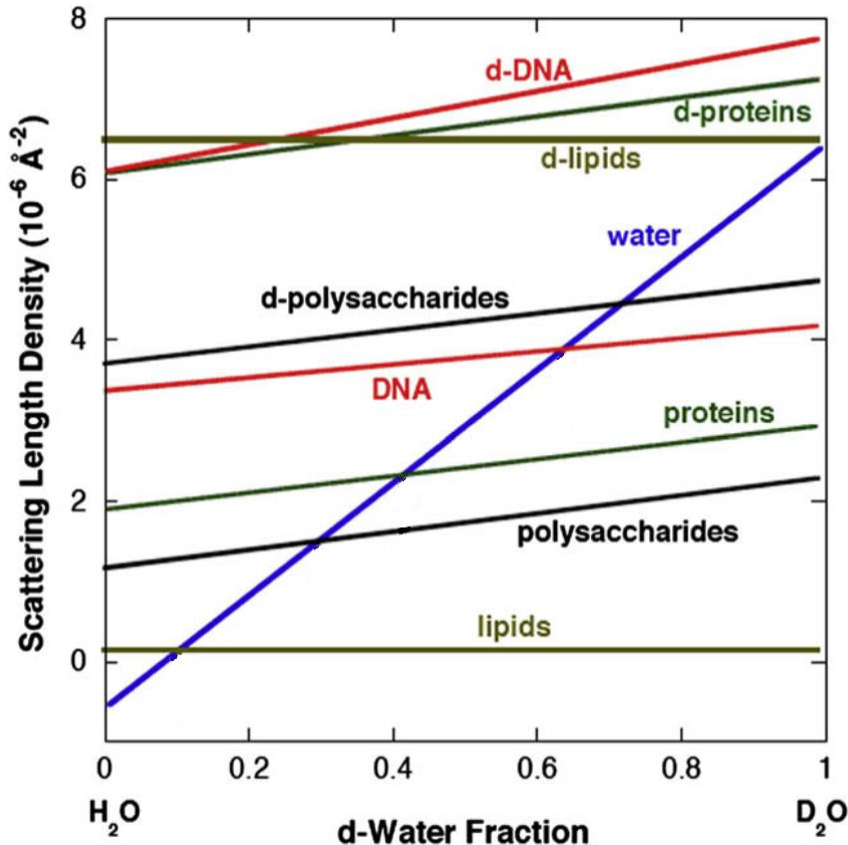


Figure 7 Dependence of scattering length density as a function of fraction of deuteration. Mixtures of ordinary and heavy water can have a very large range of scattering length densities that span the values for many biological macromolecules. Adapted from Lopez-Rubio³³.

Many biological macromolecules and macromolecular assemblies do not have a uniform density profile, and the approximation of a constant average scattering length density $\Delta\rho$ for these structures is not valid. Instead, a nonuniform radial density profile must be considered. This concept is particularly important when considering biological structures such as liposomes that have a core-shell geometry. To account for the radial dependence of the scattering length density, we can write Equation 15 as:

$$I(q) = \frac{1}{V} \int_0^{\infty} (\rho(r) - \rho_{solv})^2 e^{iq \cdot r} d^3r$$

Equation 17

We note that the scattering intensity $I(q)$ is directly proportional to the square of the difference between the local scattering length density of the particle and that of the surrounding solvent ($I(q) \propto (\rho(r) - \rho_{solv})^2$). It is possible to gain insight into the radial dependence of $\rho(r)$ by varying the scattering length density of the solvent, i.e. changing the D₂O:H₂O ratio. This allows for the possibility of contrast matching between the particles and the solvent. In the simplest case, for particles with a constant scattering length density ($\rho(r) = \rho$), the scattering intensity depends quadratically on the D₂O content of the solvent, and a perfect match, corresponding to no scattering, is achieved for $\rho_{solv} = \rho$. For particles with a core-shell structure, with different scattering length densities for the core and shell, two contrast match conditions would be achieved, one for the core and another for the shell. The contrast matching concept for the core-shell geometry is illustrated in Figure 8³³.

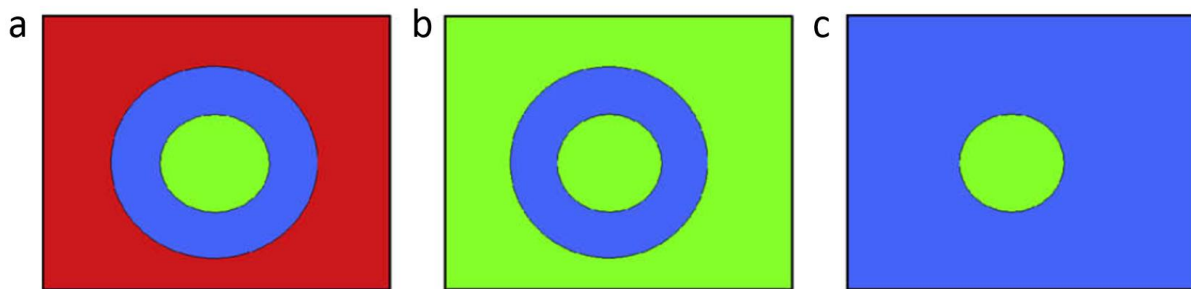


Figure 8 Illustration of contrast matching applied to a core-shell particle in a solvent. In (a), all scattering length densities are different, represented by different colours. In (b), the solvent matches the particle core, and in (c), the solvent matches the shell.

Adapted from Lopez-Rubio³³.

Therefore, performing a series of contrast matching experiments in which the D₂O:H₂O ratio is systematically varied from 0 to 1 can provide a direct, model-independent indication of the radial density profile of the macromolecules.

2.8 Small Angle Neutron Scattering

Small angle neutron scattering (SANS), in which neutrons are scattered through very small angles close to the forward direction, can be used to determine the effective diameter of particles and the particle-particle spacing in concentrated dispersions of the particles. SANS can be used if the following conditions are met:

- 1) The particles scatter isotropically (on average).
- 2) There are no long range interactions between particles.

For isotropic scattering, the factor $\langle e^{iqr} \rangle$ in Equation 16 averages to $\frac{\sin(qr)}{qr}$. The absence of long range interactions ensures that at large length scales the neutron scattering length densities (NSLD) are not correlated (ie: there is no structuring in the dispersion) and they can be expressed as the average scattering length density $\bar{\rho}$ for uniform particles.

There are model-free approaches to analyze SANS data, such as the Guinier analysis^{34,35} in which data for $qr \ll 1$ can be used to calculate the particle size. However, for the aqueous dispersions of phytoglycogen discussed in this thesis, the Guinier analysis cannot be used since the large particle size (diameters of tens of nanometers) results in $qr > 1$.

Instead, I will discuss several different models that can be used to analyze the SANS data in the present study.

2.8.1 Form Factor

Equation 17 is a general function that describes neutron scattering from a collection of particles.

It is possible to determine quantities such as the particle size and average spacing by assuming a specific form for $\rho(r)$. In the simplest model in which the particles are assumed to be uniform density spheres, $\rho(r)$ can be written as:

$$\rho(r) = \begin{cases} 1 & \text{for } r \leq R \\ 0 & \text{for } r > R \end{cases}$$

Equation 18

where R is the radius of the spheres. By substituting Equation 18 into Equation 17, one obtains an expression for the scattering intensity that corresponds to the spherical form factor of the particles³⁴:

$$P(q) = \left(\Delta\rho^2 V^2 \left[\frac{3[\sin(qR) - qR \cos(qR)]}{(qR)^3} \right]^2 \right)^2$$

Equation 19

where $\Delta\rho = \rho(r) - \rho_{solv}$ and V is the sample volume. Other more complicated radial profiles result in more complicated form factors³⁴.

2.8.2 Structure Factor

One can use Equation 16 and Equation 3 to derive a structure factor $S(q)$ ³⁶:

$$S(q) = \frac{1}{N} \left\langle \sum_{j,k} e^{iq \cdot (r_j - r_k)} \right\rangle$$

Equation 20

It is useful to remove the $j = k$ terms from the summation such that

$$S(q) = 1 + \frac{1}{N} \left\langle \sum_{j \neq k} e^{iq \cdot (r_j - r_k)} \right\rangle$$

Equation 21

In the case of liquids, for which there are no long range correlations, there are no sharp peaks in the structure factor $S(q)$. This allows the conversion of the summation to an integral that is described by a radial distribution function $g(r)$ such that

$$S(q) = 1 + \int_V e^{-iqr} g(r) dr$$

Equation 22

The radial distribution function $g(r)$ describes the variation of the density of particles with distance measured from a reference particle; specifically, it is the probability of finding a particle some distance r away from a reference particle³⁷. The shape of $g(r)$ is very sensitive to interactions between particles. For a given potential energy describing the interaction between particles, it is possible to solve for $g(r)$. It is also possible to determine $g(r)$ by performing a Monte Carlo simulation³⁷, but it is more commonly obtained by solving the Ornstein-Zernike equation that describes the direct correlation between two particles³⁸. In fluids, the Ornstein-Zernike equation is typically simplified using a closure relation known as the Percus-Yevick approximation to find the radial distribution function^{31,38-42}. For colloidal dispersions, a hard sphere model is typically assumed for which there is no interaction between particles (except when they are briefly in contact) while accounting for excluded volume. Mathematically, the hard sphere potential can be written as:

$$V(r) = \begin{cases} \infty & \text{for } r < 2R \\ 0 & \text{for } r \geq 2R \end{cases}$$

Equation 23

where r is the center-to-center distance between particles and R is the radius of the spheres. This potential can be used to obtain an analytical solution to the Percus-Yevick approximation and therefore the radial distribution function.

2.9 Quasielastic scattering

To study dynamical processes using neutron scattering, inelastic and quasielastic scattering techniques are used. Submicron electron volt resolution (μeV) is obtained by using a $\theta \approx 90^\circ$ scattering geometry as the range of wavevectors from a divergent beam is minimized⁴³. For the case of particles on a periodic lattice, we consider the total derivative of the Bragg equation to obtain:

$$\frac{\Delta\lambda}{\lambda} = \frac{\Delta d}{d} + \cot\theta\Delta\theta$$

Equation 24

For $\theta = 90^\circ$, the second term on the right hand side of Equation 24 vanishes, and the wavelength resolution is determined only by fluctuations in the lattice spacing d .

In an inelastic scattering event, in which the incident neutron scatters from an excitation of the sample, the scattered neutron has a slightly different wavelength than the incident neutron. We can also define a corresponding energy transfer ϵ . A schematic representation of a spectrum from an inelastic scattering experiment is shown in Figure 9, in which the dynamic structure factor $S(q, \epsilon)$ is plotted as a function of ϵ . There are three main features in the spectrum: 1) a large central elastic peak, which corresponds to zero change in wavelength and no energy transfer; 2) two inelastic peaks, which correspond to scattering from an excitation with energy ϵ ; and 3) a symmetric quasielastic broadening of the central peak, for which ϵ is very close to 0, characterizing the fluctuations in the average spacing of the particles, i.e. the diffusion of the

particles. By fitting Lorentzian distributions to the quasielastic broadening, the best-fit decay constant can be used to determine the diffusion coefficient, providing a measure of the dynamics of the particles in the sample.

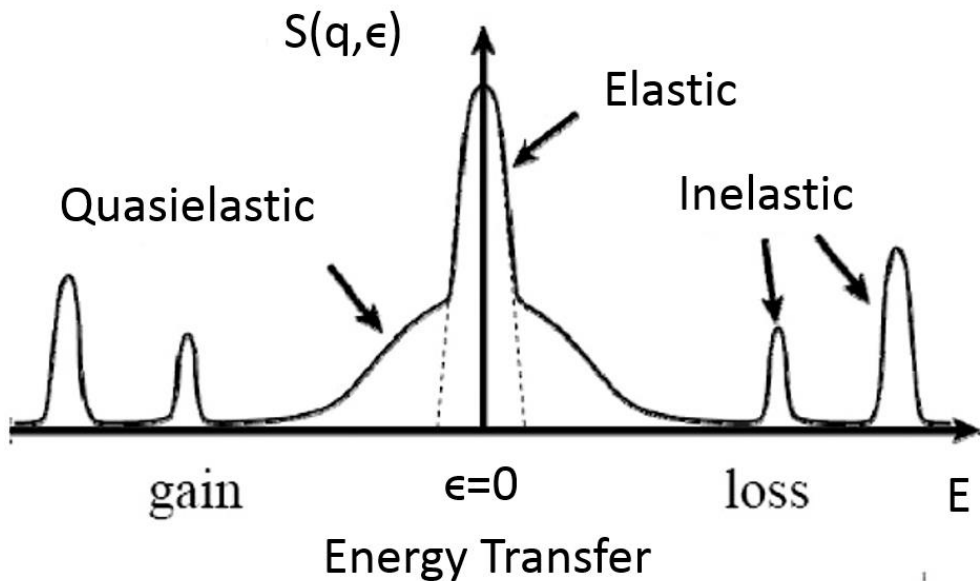


Figure 9- Generic spectrum of a backscattering experiment. The elastic region is characterized by Bragg scattering, inelastic peaks characterize neutron capture or release and the quasielastic peak characterizes the diffusion of the particles about their equilibrium positions. The shape of the broadening can be fit to a superposition of Lorentzian distribution.

It is also possible to infer changes in the dynamics of the solvent in response to changes in environmental conditions, e.g. temperature, by measuring decreases to the scattering intensity of the central elastic peak. If the data are normalized to the total number of incident neutrons, then the area under each spectrum will be constant. If dynamics are enhanced, more quasielastic scattering occurs, and this increase in the broadening requires a decrease in the intensity of the elastic peak to conserve the total intensity. Thus the observation of a decrease in the normalized

intensity of the elastic peak can be interpreted as an increase in the broadening of the quasielastic feature.

Chapter 3

Materials, Methods and Analysis

3.1 Sample Preparation

3.1.1 Purification

Phytoglycogen nanoparticles were extracted from sweet corn and purified using microfiltration techniques and generously supplied by Mirexus Biotechnologies Inc. (Satorius Stedium Biotech, 3021860604O-SG). The microfiltration procedure removed fibrous material, as well as most of the proteins and lipids. To ensure the highest purity of the phytoglycogen samples used in the present study, we further purified the nanoparticles using ultrafiltration.

Tangential flow filtration (also known as cross-flow filtration) is a pressure-driven separation process in which the dispersion is directed tangential to the surface of an ultrafiltration membrane⁴⁴. The advantage of tangential flow is that the shear produced by the flow of the dispersion reduces the accumulation of particulates on the filtration membrane surface. In the present study, a peristaltic pump was used to drive the flow, and two tangential flow filters with omega modified polyethersulfone (PES) membranes (PALL, OA500C12, OA300C12) were used. PES membranes are ideal for the present project since they are hydrophilic and the pore size is well controlled and uniform. The two PALL filters had molecular weight cut-offs (MWCO) of 500 kDa and 300 kDa. The nominal pore size of the 300 kDa filter is 35 nm; the nominal pore size of the 500 kDa filter was not quoted but the value interpolated from data supplied by PALL (Figure 10) was 50-55 nm.

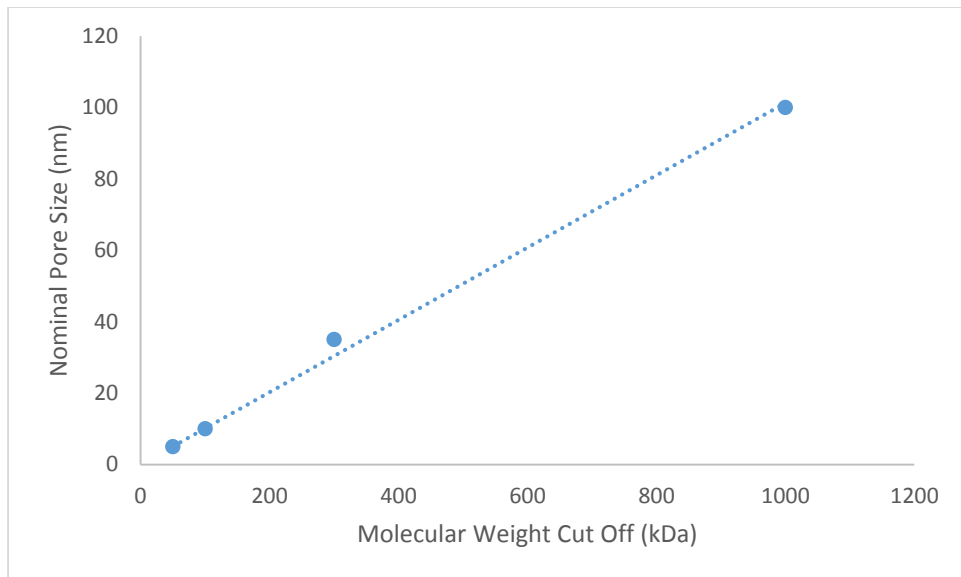


Figure 10: Nominal pore sizes for specific molecular weight cut offs were provided for their tangential flow filters on the Pall website (1). The slope is 0.101 nm per kDa, suggesting that the nominal pore size for a 500 kDa filter is approximately 50 nm.

Data adapted from Pall Corporation⁴⁴

The diameter of the phytoglycogen nanoparticles is close to the nominal diameter of the 500 kDa filter and larger than the 300 kDa filter. Because of this, the 500 kDa filter passes most of the phytoglycogen particles and removes larger particles, e.g. dust, and the 300 kDa filter will pass particles that are smaller than phytoglycogen, e.g. proteins (Figure 10). The resulting retentate from the 300 kDa filter is the ultrafiltered phytoglycogen dispersion.

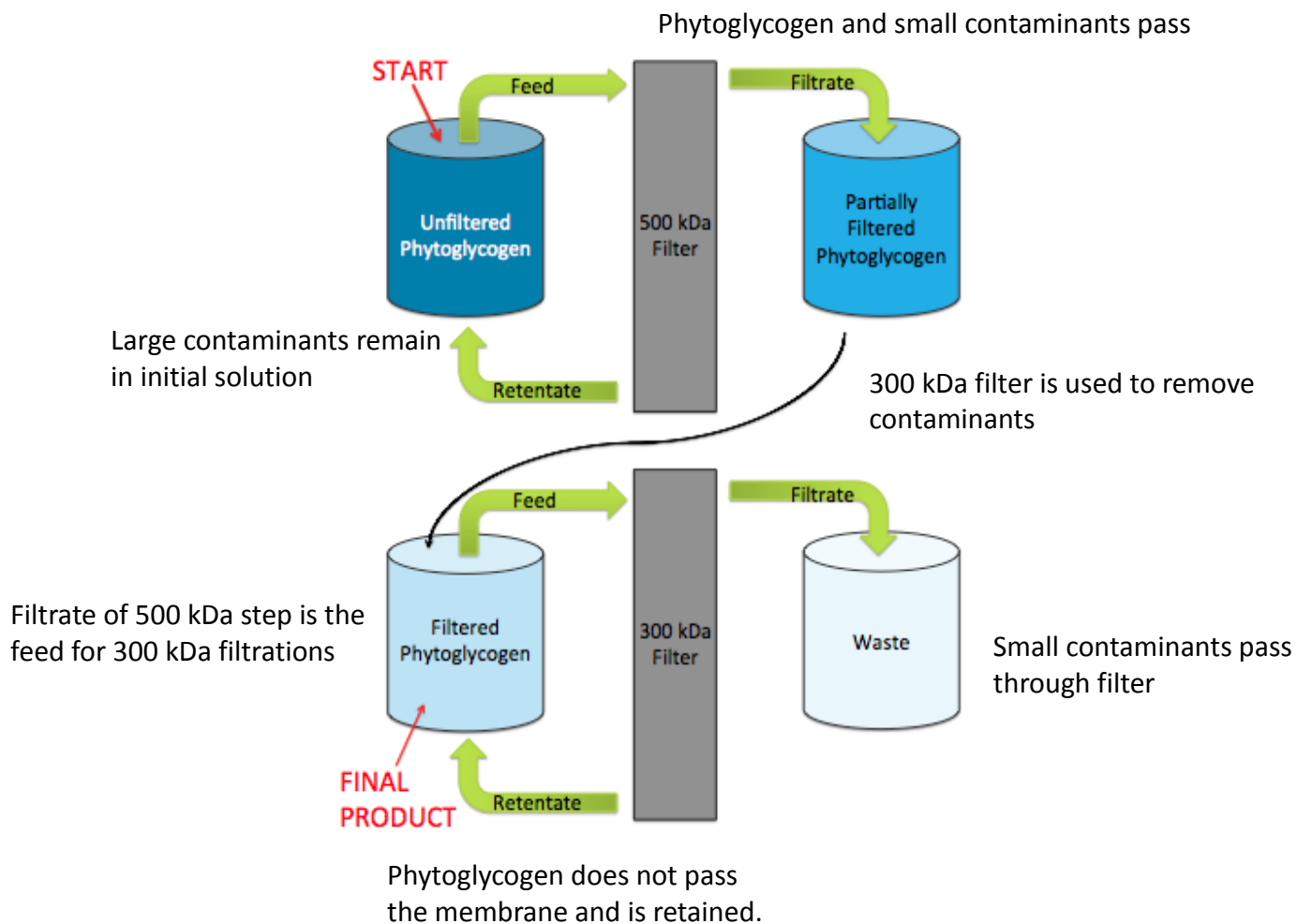


Figure 11: Schematic diagram of the phytoglycogen ultrafiltration procedure. The 500 kDa filter was used to separate the phytoglycogen nanoparticles from large contaminants in the dispersion, and the 300 kDa filter was used to concentrate the phytoglycogen nanoparticles and to remove small molecular weight contaminants. This figure was produced by Perry Mahon.

Specifically, 10 g of microfiltered phytoglycogen was dispersed in 1 L of Milli-Q water (concentration of 1 % w/w) and used as the feedstock for the ultrafiltration procedure. The dispersion was mixed using a magnetic stir bar for several hours to ensure that the phytoglycogen was completely dispersed in the water. The dispersion was flowed onto the 500 kDa filter using a peristaltic pump (Watson Marlow, 505S) using a pump speed of 95 mL/min. The feed volume was topped up with water to the initial 1 L volume whenever the volume dropped to 800 mL to dilute the dispersion for easier filtration. After generating 50 mL of the retentate, the second filtration step was stopped. The resulting dispersion was lyophilized (freeze

dried) using a lyophilizer (Heto, CT60e). The overall yield of the ultrafiltration process is ~20% (mass of output ultrafiltered phytoglycogen divided by mass of input microfiltered phytoglycogen multiplied by 100%).

3.1.2 Bradford Assay for Determining Protein Concentration

To confirm the purity of the product of the ultrafiltration procedure, we performed the Bradford protein binding assay⁴⁵. This is a simple colorimetric assay for measuring the total protein concentration with a protein sensitivity of 1 µg/mL⁴⁶. In the presence of protein, the Bradford reagent changes the colour of the solution from reddish-brown to brilliant blue. The degree of the transition to blue depends on the protein concentration and can be measured by monitoring the absorption of red light ($\lambda = 595$ nm).

A standard protein was used to calibrate the assay. There are several possible choices of protein, with both immunoglobulin G (IgG) and bovine serum albumin (BSA) recommended by Bio-Rad⁴⁶. We chose BSA as it is compatible with our water solvent and yielded a linear dependence of optical density on protein concentration at the lowest detectable limit of the assay.

An ultraviolet-visible (UV-Vis) spectrophotometer (Varian, Cary 300 Bio) was used to measure the absorbance at $\lambda = 595$ nm. To create the calibration curve, BSA concentrations of 0, 1.25, 2.5, 3.75, 5, 10, 15, 20, 25 µg/mL were prepared in mixtures of Milli-Q water (800 µL) and Bradford reagent (200 µL)⁴⁶. The mixture without added BSA was used to obtain a reference baseline and each BSA concentration was measured in triplicate and averaged. Data obtained for BSA concentrations greater than 10 µg/mL were discarded as the absorbance as a function of

protein concentration became nonlinear due to saturation of the signal at the highest concentrations.

3.2 Dynamic Light Scattering

Dynamic light scattering (DLS) measures the hydrodynamic radius r_H of colloidal dispersions in solution. A monochromatic laser is focused on a small volume element of a dispersion and its diffraction pattern recorded. As time progresses particles diffuse throughout the dispersion and changes in the diffraction pattern are recorded to produce an autocorrelation function (ACF)⁴⁷. The ACF is a measure of how similar a system is to itself at a certain time later, and it decays at a rate that depends on the particle's diffusion. At a small time step the ACF ≈ 1 as there has been minimal time evolution and, at later times, it will decay to zero as the system loses correlation. The best-fit decay constant $\bar{\Gamma}$ of the ACF is a direct measure of the diffusion coefficient D of the particles through Equation 25, where q is the scattered wavevector transfer⁴⁷.

$$\bar{\Gamma} = q^2 D$$

Equation 25

For a spherical particle the diffusion coefficient D is related to the hydrodynamic radius r_H of the particle through the Stokes-Einstein relation⁴⁸ ($D = kT/6\pi\eta r_H$, k is the Boltzmann constant, temperature T , solvent viscosity η , particle radius r_H). This corresponds to the determination of the radius of an equivalent sphere that diffuses at the same rate as the particle of interest. The

value of r_H is typically larger than the actual radius of the particle of interest because of water that is carried along with the particle.

Dynamic light scattering (DLS) experiments were performed to determine the size distribution of the phytoglycogen nanoparticles using a dynamic light scattering spectrometer (Brookhaven, BI-200SM, laser wavelength $\lambda = 532$ nm, laser power of 50 mW) with a TurboCorr autocorrelator/crosscorrelator/signal processor (Brookhaven, BI-CrossCor) (Figure 12). Dilute dispersions of ultrafiltered phytoglycogen in Milli-Q H₂O (concentrations ranging from 0.1 to 0.001 % (w/w)) were placed in 20 mL glass cylindrical scintillation vials. Low phytoglycogen concentrations were used to eliminate the possibility of secondary scattering. The temperature of the sample cavity was controlled to be 25 °C using a heated water bath. The sample cavity was filled with filtered decahydronaphthalene to facilitate heat transfer. Additionally, the index of refraction of decahydronaphthalene matches that of glass so that scattering does not occur at the glass-decahydronaphthalene interface. The diameter of the pinhole, placed 25 cm away from the sample, was selected such that the count rate was in the range of $10^5 - 10^6$ counts per second; this resulted in a large signal-to-noise without saturating the photomultiplier detector. Autocorrelation curves were collected for run times of 5 min to obtain good statistics. The cumulant method was used to analyze the measured autocorrelation curves to obtain the distribution of phytoglycogen nanoparticle hydrodynamic radii.

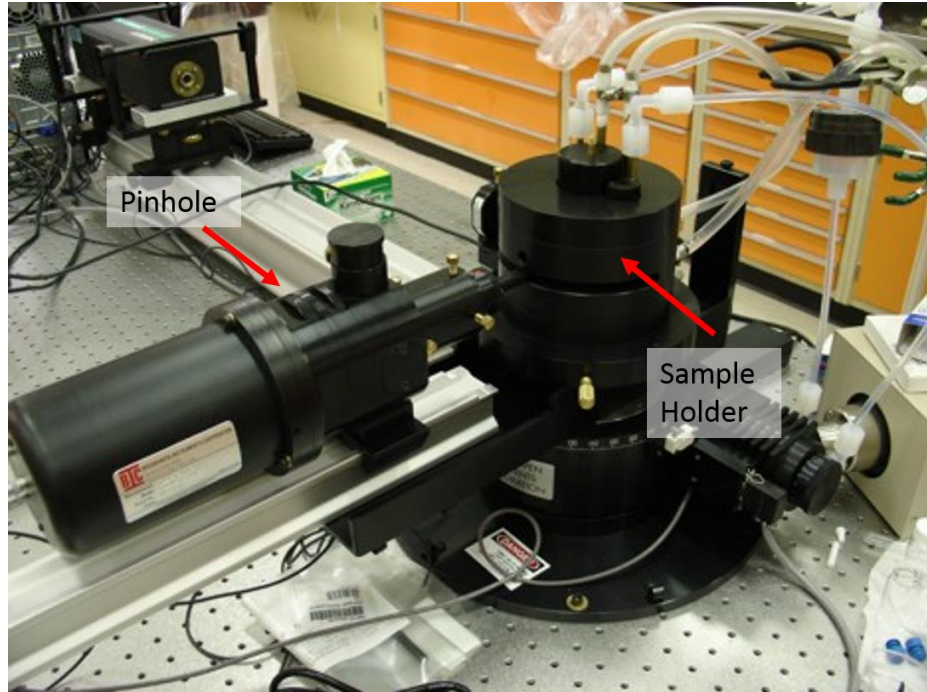


Figure 12: Brookhaven Dynamic Light Scattering Spectrometer that was used to measure the hydrodynamic radius of the phytoglycogen nanoparticles.

3.3 Neutron Scattering

SANS measurements were performed on phytoglycogen dispersions in a range of concentrations and H₂O/D₂O ratios at the Extended q-range Small Angle Neutron Spectrometer (EQ-SANS)⁴⁹, which is located at the Spallation Neutron Source (SNS) [Oak Ridge National Laboratory (ORNL)]. Samples were loaded in 2 cm diameter, 1 mm thick circular quartz cells (Hellma), which were then placed in a temperature regulated 45-position sample holder. Data were collected in 60 Hz mode using three instrumental configurations, namely: 1.3 m sample-to-detector distance, using 5.5-9 Å wavelength neutrons; 4.0 m sample-to-detector distance using 10 - 13.4 Å and 4.0 m sample-to-detector distance using 12.5 - 15 Å neutrons. These three setups yielded a total usable *q*-range between ~0.005 to 0.35 Å⁻¹. Two-dimensional scattering data were reduced using the Mantid⁵⁰ software environment and were normalized to a Porasil standard to

establish an absolute scale. Data were corrected for pixel sensitivity, dark current, and sample transmission. Background scattering from the respective solvents was subtracted from the one-dimensional intensity versus q data.

Scattering data was analyzed in three ways; (1) the total scattering invariant, Q^* , to obtain information about particle density and monomer volume, (2) the form factor, $P(q)$, for particle shape and size, and (3) the structure factor, $S(q)$, for inter-particle spacing. The total scattering invariant was evaluated from scattering measurements made in the q -range from $0.005 \text{ \AA}^{-1} < q < 0.07 \text{ \AA}^{-1}$, according to;

$$Q^* = \int q^2 I(q) dq$$

Equation 26

Subsequent analysis of $P(q)$ and $S(q)$ begins by considering the scattered intensity to be

$$I(q) = S(q)P(q)$$

Equation 27

where $S(q)$ reflects the scattering from interparticle interference, $P(q)$ reflects the form factor and contains the scaling factors, and constant background describes the q -independent incoherent background. The form factor describes the sample structure and scales with the difference in neutron scattering length density, ρ , between the solvent and particle. This implies that the total

scattering is expected to follow a ρ^2 dependence for systems with uniform neutron scattering length density (NSLD). Fits to the SANS data were performed using the SasView package⁵¹.

Dynamics measurements were made on dispersions of phytoglycogen at 10.5%, 19.7%, and 24.4% w/w in D₂O, as well as pure D₂O, in the temperature range of 100 K to 300 K. The Backscattering Spectrometer (BASIS)⁵² at SNS was used for QENS measurements in an energy range of $\pm 120 \mu\text{eV}$, with a resolution of 3.5 μeV and a q -range of 0.2 – 2.0 Å⁻¹. BASIS was also used to obtain elastic fixed window scattering data at a resolution of $\pm 3.5 \mu\text{eV}$. The Cold Neutron Chopper Spectrometer (CNCS)⁵³ at (SNS) was used for measurements of D₂O at 295 K in the energy range up to $\sim 47 \text{ meV}$, with a resolution of $\sim 50 \mu\text{eV}$ in the q -range from 0.5 to 5 Å⁻¹. All BASIS and CNCS spectra were corrected for a background and sample holder, and were normalized to the scattering from vanadium. No multiple scattering corrections were used. Data reduction for BASIS spectra was performed using the Mantid⁵⁰ software environment and fitted in intensity using the DAVE software suite⁵⁴.

Chapter 4

Results and Discussion

4.1 Bradford Assay

To obtain a measure of the purity of the ultra-filtered phytoglycogen dispersions, we performed the Bradford protein assay. The calibration curve for this assay is shown in Figure 13. The data follows a linear trend indicating that BSA is a suitable standard for the Bradford assay and can be used to measure the total protein concentration down to a total protein concentration of 1.25 µg/mL. For dispersions of the ultra-filtered phytoglycogen with concentrations of 0.1% and 0.01% (w/w), the absorbance values were 0.0222 and 0.0018, respectively. These values are below the detection limit of the assay and are comparable to the values measured for pure water. Based on this result, it is possible to determine an upper limit on the total protein concentration in the phytoglycogen dispersions of 0.1%.

It should be noted that dispersions of the micro-filtered phytoglycogen obtained from Mirexus Biotechnologies Inc. had absorbance values similar to those of dispersions of the ultra-purified phytoglycogen, demonstrating that the micro-filtration procedure removes most of the protein.

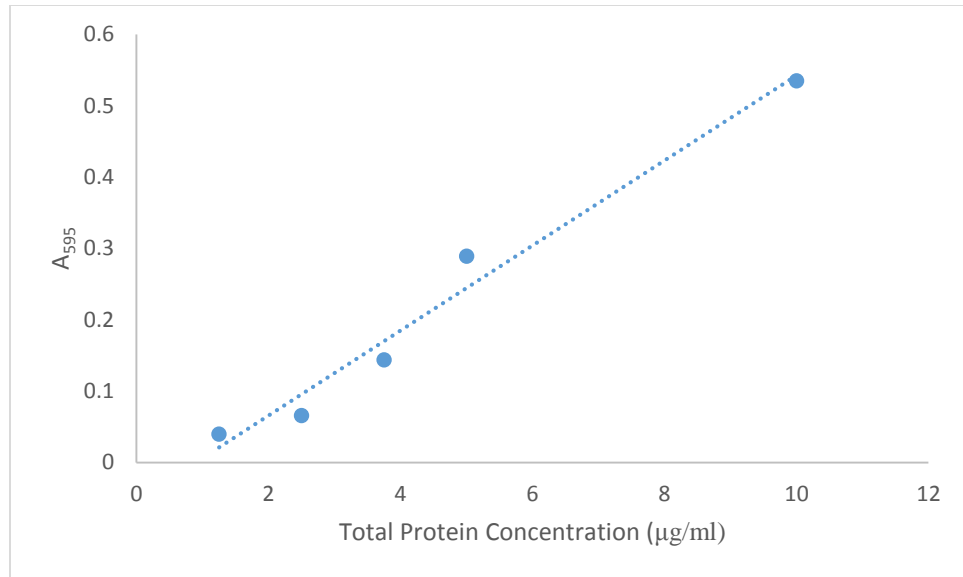


Figure 13: Calibration curve for the Bradford protein assay measured using a bovine serum albumin (BSA) standard, showing the absorbance of light (at $\lambda = 595$ nm) versus total protein concentration. The best-fit straight line can be used to relate the measured absorbance to the total protein concentration.

4.2 Dynamic Light Scattering

The autocorrelation function for a 0.001% w/w dispersion of phytoglycogen in water is shown in Figure 14 , corresponding to a best-fit value of the hydrodynamic radius r_H of 34.9 nm with a polydispersity index of 0.067, validating the monodispersity of phytoglycogen. The measured hydrodynamic radius is approximately twice that of that measured using small angle neutron scattering. This discrepancy is likely due to the complicated nature of light scattering from highly branches particles^{2,55}.

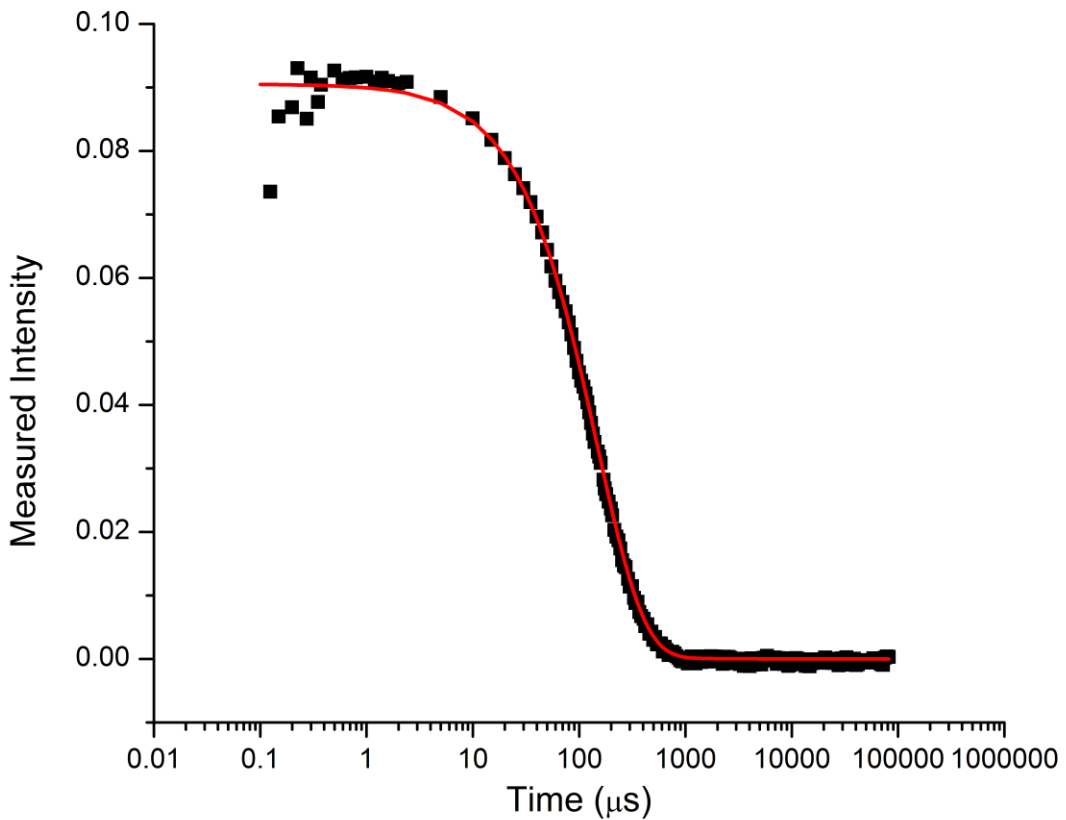


Figure 14 Autocorrelation function for a dispersion of ultra-filtered phytoglycogen in Milli-Q water with a concentration of 0.001% w/w. The best-fit value of the hydrodynamic radius $r_H = 34.9$ nm with a polydispersity index of 0.067.

4.3 Neutron Scattering

4.3.1 SANS Structure, Spacing, Hydration Water and Molecular Weight

The first level of structural characterization involves using SANS to study dispersions of phytoglycogen in 100% D₂O as a function of concentration (0% to 24.4% w/w) at 295 K. We found that the low concentration data (1.0% w/w) was best fit using a sphere of uniform density and a Shultz distribution for polydispersity⁵⁶. We also considered a number of other form factor

models (sphere of uniform density, core shell, and sphere with continuous changes in NSLD), and found that the data was best fit using this a sphere of uniform density. This is also supported by the contrast series experiments that indicate a uniform NSLD (Figure 16). Fitting of the SANS data allowed the determination of the radius and NSLD of phytoplasmal glycogen particles in 100% D₂O: 17.4 ± 1.6 nm and $0.58 \text{ fm}/\text{\AA}^3$ respectively. This particle radius is smaller than but comparable to the particle size measured by AFM, electron microscopy, light scattering, and size exclusions chromatography^{1,16,57,58}. The discrepancy could be because the SANS measurement is performed on the particles in dispersions in the absence of strains, interaction with an underlying substrate, or by using dynamical properties to infer the particle size.

At higher concentrations, SANS is sensitive to particle-particle correlations³⁹. This results in a structure factor, $S(q)$, that modifies the scattering intensity. According to Equation 27, dividing the high concentration data by data from a relatively dilute (1% w/w dispersion) that does not contain scattering from inter-particle interference, reveals the structure factor (Figure 15b). One should note, that this approach assumes that there is no change in the particle size as a function of concentration, which appears to be valid based on the analysis that the particle density does not change with concentration (Figure 16c). We subsequently fit the structure factor using a hard sphere model³⁸ to calculate the inter-particle spacing (Figure 15c). This analysis reveals that the inter-particle spacing approaches the average diameter of the phytoplasmal glycogen particles near our maximum concentration of 24.4% w/w. This result is consistent with the onset of a jamming transition^{59,60}, which is observed as a marked increase in the zero shear viscosity of phytoplasmal glycogen dispersions at a concentration of ~25% w/w (Figure 2).

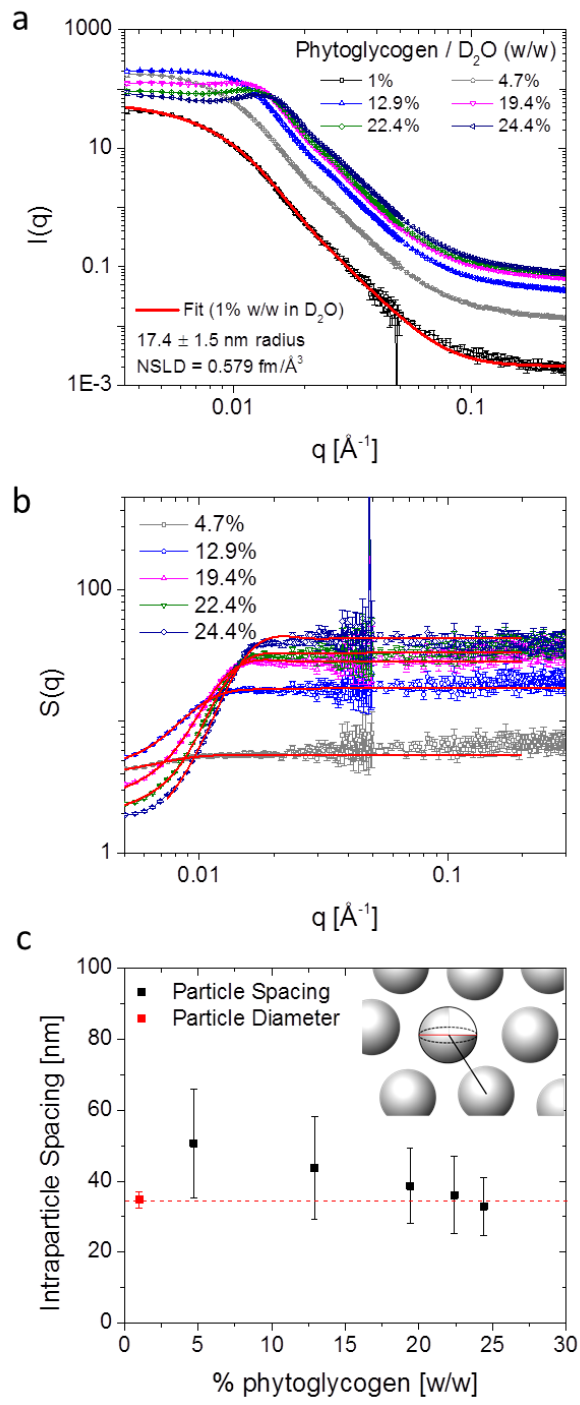


Figure 15 SANS results of phytoglycogen dispersions. (a) Scattering intensity versus scattering wavevector q as a function of concentration. The lowest concentration data was fit to obtain the radius and scattering length density of the phytoglycogen particles (error reported is σ^2). (b) The emergence of a structure factor from inter-particle scattering used to determine inter-particle distance (c), which approaches the particle diameter at 24.4% w/w. This is also consistent with the onset of jamming observed from rheological studies of the dispersions.

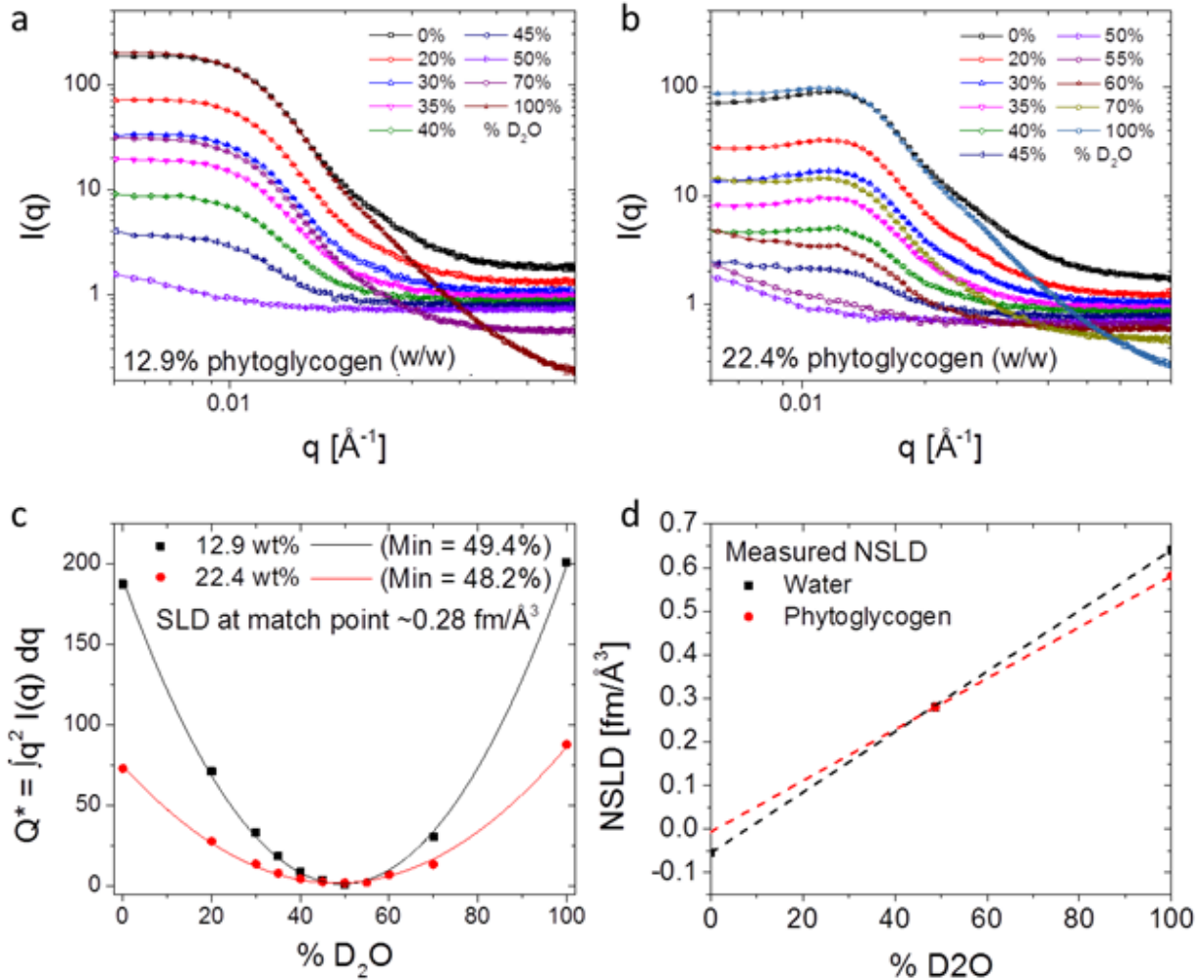


Figure 16 Neutron contrast series used to establish the NSLD of phytoglycogen. SANS for two phytoglycogen concentrations: (a) 12.9% w/w and (b) 22.4% w/w, for different % D₂O. (c) The total scattering, as indicated by the Porod invariant Q^* , shows a clear minimum that is independent of concentration. (d) Contrast matching used to predict the scattering length density of the phytoglycogen particle as a function of H₂O/D₂O ratio.

Because neutrons scatter differently from hydrogen and its heavy isotope deuterium, we have performed SANS measurements on dispersions of two phytoglycogen concentrations (12.9% and 22.4%) as a function of different H₂O/D₂O ratios (Figure 16). This type of experiment is commonly referred to as a contrast series. The contrast series data shown in Figure 16 provide three pieces of information. Firstly, the match point in the NSLD of phytoglycogen, occurs at 48.8% D₂O. Secondly, the match point did not change significantly with concentration (Figure 16c), showing that there was no change in particle density as the separation between particles

was significantly decreased. Finally, the data demonstrated a roughly uniform density of the phytoglycogen particles, as implied by the quadratic shape of the Porod invariant Q^* vs. % D₂O (Figure 16c). This arises from the dependence of intensity on the square of the difference in the NSLD of the particle and the solvent ($Q^* \propto (\Delta\rho)^2$). The quadratic shape suggests that there is a linear relationship between the NSLD of the particle and the solvent (Figure 16d). This finding reaffirms our use of the hard sphere model for the form factor of the particle, a model which is consistent with the uniformly dense structure associated with phytoglycogen particles^{18,19,27}.

Determining the match point of the system allows us to calculate the volume of the glucose monomers within the phytoglycogen particle. Dividing the sum of the atomic scattering lengths²⁹ b_i for the average monomer dissolved in 48.8% D₂O (C₆H_{8.54}D_{1.46}O₅) by the match point NSLD (0.28 fm/ Å³), results in a molecular volume per glucose monomer of 167 Å³. This in turn allows us to calculate the water content of the fully hydrated phytoglycogen particle. We do this by estimating the hydration number n_H , which is the number of water molecules associated with each glucose monomer that are required to obtain the best-fit NSLD value at 100% D₂O (0.58 fm/Å³). This is done using the definition of NSLD at 100% D₂O:

$$NSLD_{100\%D_2O} = \frac{b_{phytoglycogen} + b_{D_2O}n_H}{v_{phytoglycogen} + v_{D_2O}n_H}$$

Equation 28

where v_{D_2O} is taken to be 30.4 Å³⁶⁰. Additionally, we note that exchangeable protons within the glucose monomers must be taken into account, which changes the value of $b_{phytoglycogen}$ from 46.7 fm at 48.8% D₂O, to 62.7 fm at 100% D₂O. Solving Eq. 3 for n_H , we find that it would take 22.5

± 2.5 water molecules per glucose monomer to reach an NSLD of $0.58 \text{ fm}/\text{\AA}^3$ in 100% D₂O. Furthermore, we can use the SANS data to obtain an estimate of the molecular weight of the phytoglycogen particles. We calculate the number of glucose monomers per particle, $n = 2.60 \times 10^4$, by dividing the total particle volume, $2.21 \times 10^{-23} \text{ m}^3$, by the average volume per monomer (including the associated water), $8.51 \times 10^{-28} \text{ m}^3$. By multiplying the number of monomers by the monomer molecular weight, 162 g/mole (based on the formula C₆H₁₀O₅ for particles in H₂O), we obtain the molecular weight of a completely dry phytoglycogen particle as 4.21×10^6 g/mole. Including the mass of 22.5 water molecules per glucose monomer yields a molecular weight of 14.7×10^6 g/mole for phytoglycogen particles fully hydrated in H₂O, with each particle containing approximately 250% of its mass in water. We note that there are a number of assumptions made in this analysis, such as assuming that the volume of hydration water is unchanged from that of bulk water, and that hydration water does not change substantially with deuteration. We also note that the analysis of the data from the quasielastic neutron scattering measurements—which we describe below—yields a similar value for the hydration number n_H .

4.3.2 Elastic and Quasielastic Dynamics

Quasielastic neutron scattering (QENS) experiments provide a probe of the dynamics of the water solvent in the presence of the phytoglycogen nanoparticles. These data have been analyzed in several ways, and we begin with a discussion of elastic fixed window scan experiments that provide a rapid probe of dynamics occurring at a set timescale. Our measurements on BASIS are sensitive to atomic motions occurring faster than 800 ps within the q-range of 0.2 to 2.0 Å⁻¹ (~3-

30 Å in real space). The data in Figure 17 represents the fraction of neutrons scattering elastically from atoms that do not move the distance defined by the q-vector within 800 ps. We normalize the observed total scattered intensity at a given temperature to that measured at low temperature (100 K in our case), where atomic motions are significantly reduced. The data reveal dynamical onsets and phase transitions as the temperature increases.

Fixed window elastic scattering data were collected for D₂O and phytoglycogen dispersions in D₂O at 10.5%, 19.7%, and 24.4% w/w, at temperatures from 100 K to 300 K (Figure 17). The predominant feature in the data is an abrupt decrease in the elastic scattering corresponding to the melting of bulk D₂O at 277 K. There is also a decrease in elastic scattering immediately below this transition, specifically at high q and high phytoglycogen concentrations, indicative of changes in dynamics arising from the presence of phytoglycogen particles. Close inspection of the data above the melting transition reveals increased elastic scattering with increasing phytoglycogen concentration, reflecting a larger amount of scattering from the phytoglycogen particle and its associated hydration water, which is slower than bulk water. These data confirm that there is a measureable effect of phytoglycogen concentration that can be probed with quasielastic scattering measurements, providing a more complete picture of the system dynamics.

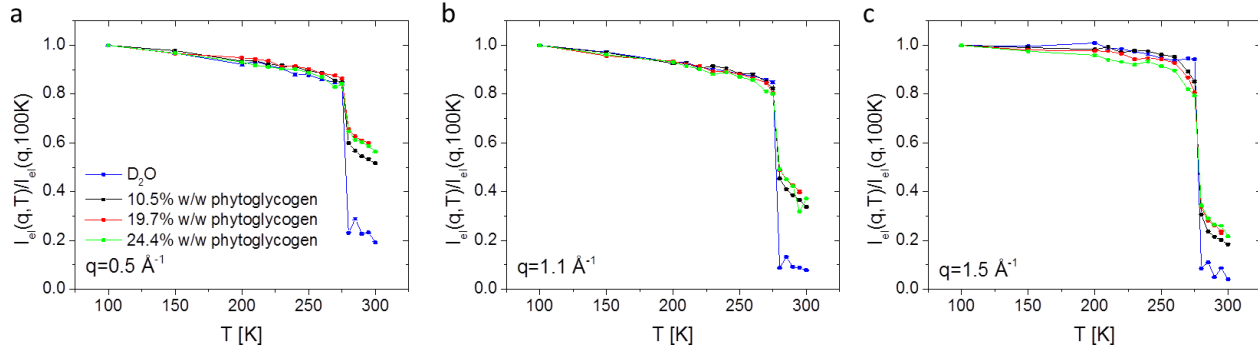


Figure 17 Fixed window elastic scattering data at (a) $q = 0.5 \text{ \AA}^{-1}$, (b) $q = 1.1 \text{ \AA}^{-1}$, and (c) $q = 1.5 \text{ \AA}^{-1}$ as a function of temperature from 100 K to 300 K. The transition at 277 K corresponds to the melting of bulk D_2O . Increased elastic scattering at higher concentrations reflects the decreased relative contribution from bulk water.

We obtained QENS spectra for aqueous (D_2O) dispersions of phyto-glycogen at concentrations of 0% (bulk D_2O), 10.5% w/w, 19.7% w/w and 24.4% w/w, and temperatures of 100 K, 280 K, and 295 K. By summing across the entire q -range, we obtain a picture of the dynamics in the 30-800 ps timeframe. It is informative to show this excess in the quasielastic scattering as the imaginary part of the susceptibility, which is calculated as:

$$\chi''(q, E) = \frac{S(q, E)}{n_B(T, E)} = S(q, E) * \left[e^{\frac{E}{k_B T}} - 1 \right]$$

Equation 29

where n_B is the temperature dependent Bose occupation number. In Figure 18 we show QENS spectra for phyto-glycogen dispersions of different concentrations superimposed on spectra for D_2O , to demonstrate the presence of additional processes in the presence of phyto-glycogen. Excess scattering as a function of concentration is evident at lower energy transfers. Prior

analysis of oligo- and polysaccharide solutions⁶¹ suggests that these data can be treated as three dynamic processes, namely bulk water translation, hydration water translation, and the tail of a relaxation associated with the sugar.

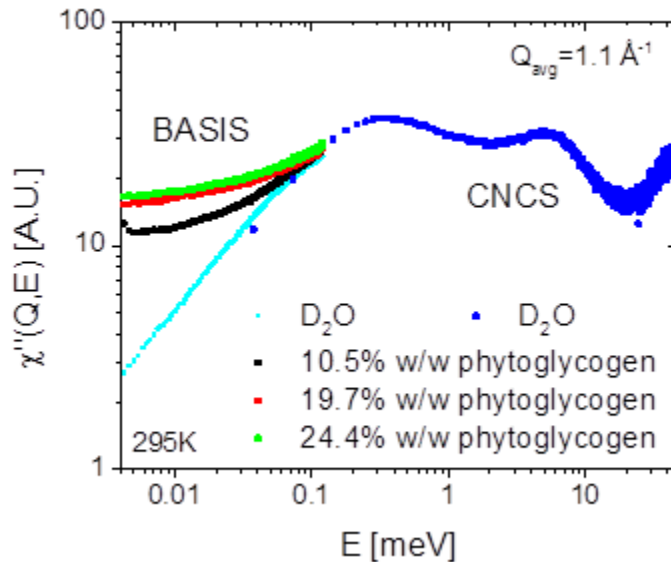


Figure 18 QENS data for phytoglycogen dispersions as a function of concentration presented as dynamic susceptibility χ'' at 295 K, with the data summed over all q . The BASIS data are superimposed on spectra of bulk D_2O data from BASIS and CNCS. This overlay of data illustrates the excess scattering from the dynamics of hydration water and the phytoglycogen particles relative to that of bulk D_2O .

Based on this, we can perform a more detailed analysis of the QENS data as a function of scattering wavevector q by presenting the data as the dynamic structure factor $S(q,E)$. The data can be fit using Lorentzian functions $\Gamma(q,E)$ to represent the inelastic scattering of the various dynamical processes, while the elastic scattering terms are represented by a delta function $\delta(E)$ ⁶². The elastic component is scaled by the Elastic Incoherent Structure Factor or $EISF(q,E)$ associated with each process, and is defined as the ratio of elastic intensity to total scattered intensity. From these terms we can construct the theoretical scattering function:

$$S_{Theo}(q, E) = \sum_{i=1}^n P_i(EISF_i(q)\delta(E) + [(1 - EISF_i(q)) * \Gamma_i(q, E)]$$

Equation 30

which can be fit against experimental data as follows:

$$S_{Exp}(q, E) = DWF(q) * [S_{Theo}(q, E) \otimes R(q, E)] + B(q, E)$$

Equation 31

$R(q, E)$ is the instrument resolution function, taken from a low temperature (100 K) measurement of each sample, $B(q, E)$ is the instrument background, and $DWF(q)$ represents the Debye-Waller Factor (an example of the fit is shown in Figure 19a). Analysis of the dynamic structure factor provides the full-width at half-maximum (FWHM) (Figure 19b and Figure 19c) and the normalized amplitude terms a_i (Figure 20a and Figure 20b) of the Lorentzian functions associated with each of the dynamic processes. Each FWHM term is related to the relaxation time of the corresponding dynamic process, while the amplitude terms are associated with the relative contributions of each process.

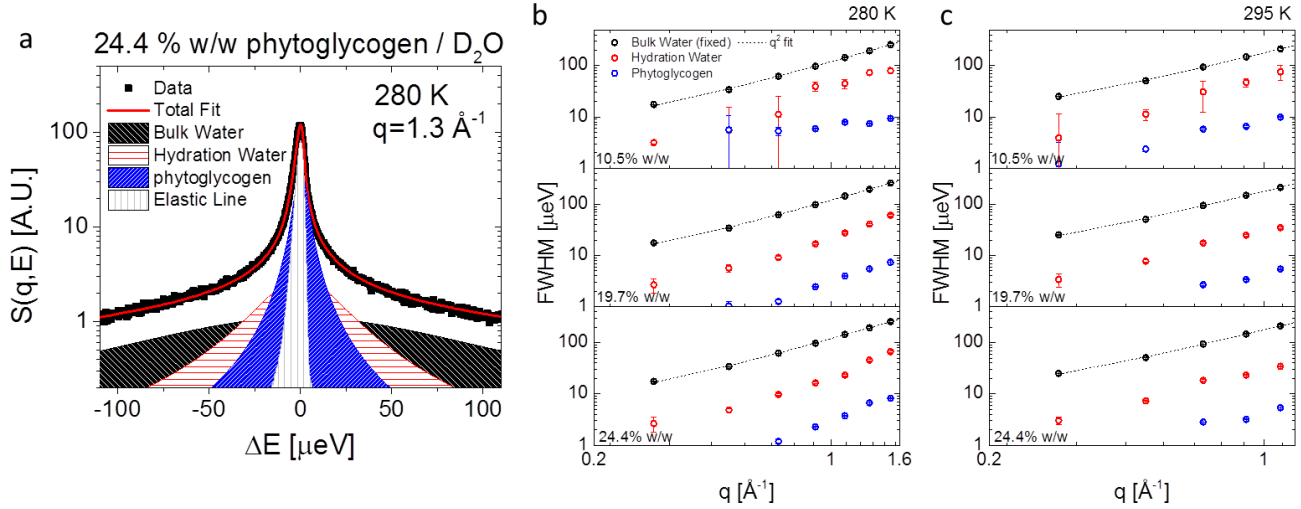


Figure 19. Fitting of QENS data. (a) A sample fit is shown for 24.4% w/w phytoglycogen in D_2O at 280 K for $q = 1.3 \text{ \AA}^{-1}$. The fit requires three Lorentzian functions in addition to the instrumental resolution function to account for the elastic scattering. The FWHM for each Lorentzian component is shown for data collected at (b) 280 K and (c) 295 K. The q -range is truncated due to processes leaving the dynamic window of the instrument (errors reported are σ^2).

As suggested above, fitting the data requires three inelastic components, with the first two Lorentzian components representing the translational diffusion of bulk and hydration water, respectively. The FWHM of the bulk water term is fixed from our fitting of the D_2O spectra collected at 280 K and 295 K, while the hydration water term is permitted to vary. All the amplitudes are free parameters. The water spectra were fit with a single Lorentzian function, which reproduced the data well in the q -ranges of $0.2 - 1.6 \text{ \AA}^{-1}$ at 280 K, and $0.2 - 1.2 \text{ \AA}^{-1}$ at 295 K. Accordingly, we restricted our analysis of all other samples to these q -ranges. Additionally, the use of Lorentzian functions to fit the water dynamics is not ideal, as both bulk and hydration water relaxations are known to exhibit a nonexponential behavior⁶³⁻⁶⁶. The third Lorentzian feature is assigned to the tail of the phytoglycogen relaxation. This analysis is similar to that used for oligo- and polysaccharide spectra obtained from depolarized light scattering that show comparable intensity in the range of 1 - 100 GHz (0.004 – 0.4 meV)⁶¹. We do not present a detailed analysis of the phytoglycogen process used in the fitting of the QENS data to avoid

over-interpretation of the data, since the majority of this process resides outside of our experimental window. However, it is reasonable to expect a contribution of side-chain dynamics of the phytoglycogen contributing to the low energy side of the spectra^{61,67,68}.

There is also a clear trend in the relative amplitude terms of bulk and hydration water as a function of phytoglycogen concentration. As the concentration is increased, a larger fraction of the water population is needed to hydrate the particles; this is reflected in the decrease of $a_{\text{Bulk Water}}$ and a corresponding increase in $a_{\text{Hydration Water}}$, as seen in Figure 20. We will return to this relationship between the hydration and bulk water contributions, using it to provide an independent estimate of the hydration water content.

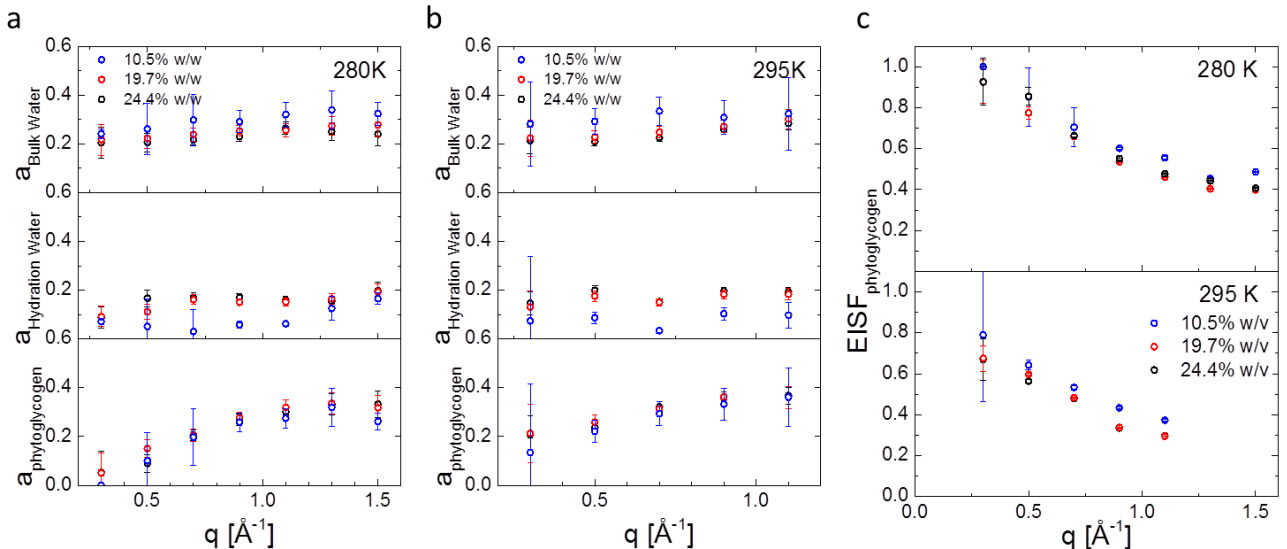


Figure 20 Fitting of QENS data. Normalized area terms a_i for each of the Lorentzian functions used to fit the QENS data at (a) 280 K and (b) 295 K. No q -dependence is observed in the relative contributions of the water components, but the phytoglycogen process shows increasing intensity as a function of q . The EISF of the process assigned to phytoglycogen is presented in (c). This shows no significant dependence on concentration at either 280 K or 295 K indicating that the geometry of the phytoglycogen motions is unaffected by crowding in this concentration range (errors reported are σ^2).

The FWHM values for bulk water show the expected q^2 dependence associated with translational diffusion, while that for the hydration water shows an average q -dependence of q raised to the

power 2.6 ± 0.3 (Figure 21). This indicates that the motions of hydration water are sub-diffusive, consistent with other neutron measurements of hydration water in proteins^{63,69}. Hydration water also translates more slowly than bulk water, as seen by the smaller value of the FWHM. This perturbation is quantified as the retardation factor, ξ , defined as the ratio of the bulk water FWHM to the hydration water FWHM. Here, we report an average retardation factor of $\xi = 5.8 \pm 1.2$ for phytoglycogen, calculated across a q -range of $0.2 - 1.6 \text{ \AA}^{-1}$ at 280 K and $0.2 - 1.2 \text{ \AA}^{-1}$ at 295 K. This is comparable to the retardation factor reported for glucose, which is the monomer of phytoglycogen, and other small saccharides^{61,67,70}. It is remarkable that the dramatic increase in molecular weight and structural complexity of phytoglycogen do not drastically modify the degree of perturbation on the hydration water dynamics⁶¹. This perturbation is consistent with the effect of short range interactions between the monomer and water, where water–sugar and water–water hydrogen bonds have comparable strength⁷⁰ and the sugar molecules are able to partially replace water in the tetrahedral hydrogen bond network⁷¹.

It is important to note however, that the retardation factor has an implied dependence on q , because the motions of hydration water are sub-diffusive, whereas the motions in bulk water are diffusive ($q^{2.6}$ vs q^2). As such, any reported retardation factor should include a reference to the length scale of the dynamic process probed, and the technique used⁷². In fact, this shows the power of neutron scattering measurements, which simultaneously provide dynamical information at multiple length scales. In Figure 21b we demonstrate this by plotting the retardation factor as a function of scattering wavevector. Here we observe a clear trend in the apparent perturbation of hydration water with respect to the length scale used to interrogate the system. At low q , or long distance, hydration water dynamics are more perturbed than at shorter distances (high q).

We also report the elastic incoherent structure factor (*EISF*) for the process assigned to the relaxation of phytoglycogen. The *EISF* is used to interrogate the geometry of molecular motions, and we disregard the bulk and hydration water terms in this calculation. This is justified because the full scattered intensity of bulk and hydration water diffusion is represented by Lorentzian functions in the experimental window, meaning that they do not contribute to the elastically scattered intensity. Accordingly, any residual elastic intensity is assigned to the phytoglycogen process, and the *EISF* can be computed as:

$$EISF_{phytoglycogen} = \frac{a_{elastic}}{a_{elastic} + a_{phytoglycogen}}$$

Equation 32

where $a_{phytoglycogen}$ is the amplitude of the Lorentzian function, and $a_{elastic}$ is the amplitude of the instrumental resolution function representing the elastic line. Again, we do not present any model for the phytoglycogen term, as it is associated with the tail of a slower relaxation process that resides outside of our experimental window. We do however wish to note that there is no change in the *EISF* as a function of phytoglycogen concentration at either of the two temperatures. Taken together with the insensitivity of the FWHM for this process as a function of concentration, this indicates that no changes in the dynamics of phytoglycogen emerge in the range of concentrations that we studied, suggesting no crowding effect with increasing concentration. This is consistent with the structural analysis in this work that showed no change in the NSLD match point (or particle density) between 10.5% w/w and 24.4% w/w.

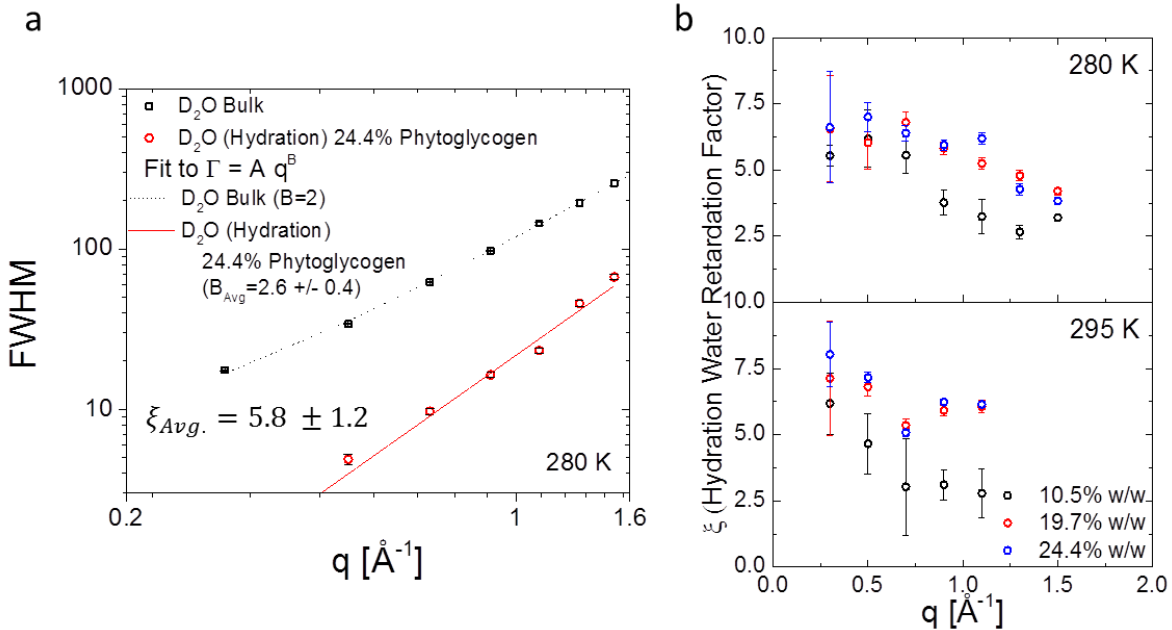


Figure 21 Example of fitting of FWHM values for bulk and hydration water translation in phytoglycogen dispersions. The exponent and retardation factor reported in (a) reflect the average value for measurements at both 280 K and 295 K at all three concentrations. (b) Retardation factors for hydration water show a clear q -dependence, reflecting the sub-diffusive nature of hydration water translation in phytoglycogen

The amplitude terms for bulk and hydration water that result from the analysis of the QENS data also permit us to calculate the number N_H of water molecules incorporated in each phytoglycogen particle using the relation:

$$N_H = \frac{f_{sol} * a_{\text{Hydration Water}}}{a_{\text{Bulk Water}} + a_{\text{Hydration Water}}}$$

Equation 33

where f_{sol} is the solute/water molar ratio^{31,38}. Taking the molecular weights of phytoglycogen and D₂O to be 4.23×10^6 g/mole and 20 g/mole, respectively, we obtain $N_H = 6.7 \times 10^5 \pm 1.2 \times 10^5$ water

molecules per phytoglycogen particle (average of all concentrations and q -values). We obtain the hydration number n_H per glucose monomer by dividing N_H by the average number of glucose monomers in the phytoglycogen particles, 2.60×10^4 . This yields a value of $n_H = 25.8 \pm 4.6$ water molecules per glucose monomer, which agrees to within error with the value of n_H obtained from our analysis of the SANS data, (22.5 ± 2.5 water molecules per glucose monomer). Taken together, these data indicate that phytoglycogen particles contain between 250% and 285% of their mass in water.

The value of the hydration number is remarkable when compared to the number of perturbed water molecules per glucose molecule in solution, which is ~ 14 , as measured by extended depolarized light scattering^{61,67}. As mentioned above, the effects of sugars on water are thought to be short range interactions with the sugar molecules partially replacing water in the tetrahedral hydrogen bond network⁷¹, perturbing only the first shell of water around glucose⁷³. For phytoglycogen, we observe between 22-26 water molecules per glucose monomer, a significantly higher value than for glucose in solution. This is better shown by comparing the number of hydration waters per free –OH group. Oligo- and polysaccharides in solution typically associate ~ 3 water molecules per –OH group^{61,67}. On the other hand, phytoglycogen has more than 7 water molecules perturbed per free –OH group. We ascribe this increased number of perturbed or ‘bound’ water to the closely packed chains within the phytoglycogen particles.

Chapter 5

Summary and Future Work

5.1 Summary of Results

We used neutron scattering to better understand the relationship between phytoglycogen and water. SANS measurements show that the nanoparticles are relatively monodisperse, with a nominal radius of 17.4 ± 1.6 nm. The particle-particle spacing that we observed suggests the dispersions approach the jamming regime at our highest measured concentration of 24.4% w/w. This is consistent with the divergence of the zero shear viscosity at concentrations greater than 25% w/w. Contrast variation experiments showed that there is no significant effect of crowding between concentrations of 12.9% and 22.4% w/w, as evidenced by their unaltered density. More interestingly, this allowed us to calculate the monomer volume (167 \AA^3), leading to an estimate of the particle hydration number (22.5 ± 2.5 water molecules per glucose monomer).

QENS measurements provided detailed information regarding the dynamics of water in phytoglycogen dispersions as a function of phytoglycogen concentration. The dominant effect of increasing concentration was an increase in the relative amount of hydration water associated with the particles. In this way, phytoglycogen shows promise as a platform for investigations of hydration water in hydrophilic environments. This allowed us to quantify not only the amount of water associated with each particle (25.8 ± 4.6 water molecules per glucose monomer), but also to quantify both the retardation of hydration water motions (5.8 ± 1.2) and the q -dependence of the translational motion of the hydration water. The translational motion of hydration water was

seen to be sub-diffusive with a q -dependence of the FWHM given by a power law exponent of 2.66 ± 0.34 , consistent with measurements of hydration water in other systems. This highlights an important reality for studies of hydration water physics, namely that the sub-diffusive nature of these motions relative to the diffusive nature of bulk water, makes the retardation factor a length scale dependent parameter.

The dendrimeric structure of phytoglycogen is markedly different from other natural polysaccharides of similar molecular weight, resulting in a significant increase in the number of associated water molecules when compared to other oligo- and polysaccharides. Fully hydrated phytoglycogen particles contain between 250% and 285% of their own mass in water. This makes aqueous dispersions of monodisperse phytoglycogen nanoparticles an ideal system for detailed testing of theories of colloidal dispersions and hydration water physics. Moreover, this highlights the intimate interactions of phytoglycogen with water that result in its unique properties such as extraordinary water retention, low viscosity in water, and exceptional stability. The insights provided into the interactions of phytoglycogen and water in this study will enable promising new technologies and therapies based on this sustainable nanomaterial.

5.2 Future Work

5.2.1 Light Scattering

In the present study, DLS measurements yielded a particle diameter that was approximately twice that measured using SANS. This unexpected result could be because of complex scattering from the hyperbranched structure of the phytoglycogen nanoparticles^{2,55}. This result needs to be studied in more detail in combination with static light scattering (SLS) measurements. SLS

provides a measurement of the radius of gyration R_g of the particles. Burchard^{2,55} has pointed out that it is important to measure both r_H and R_g for hyperbranched polymers, given the complex nature of the scattering.

5.2.2 High Resolution Imaging of Phytoglycogen Nanoparticles

Cryo-transmission electron microscopy (TEM) can be used to collect high resolution images to further characterize the size of phytoglycogen. Cryo-TEM images have been collected on glycogen with and without the use of heavy stains^{1,16} and this methodology could be used to phytoglycogen. These measurements are complicated by the interaction of the particles with the underlying surface since the particles are highly deformable. High-resolution atomic force microscopy (AFM) measurements are currently being performed in our laboratory. The AFM technique has distinct advantages: measurements can be performed in liquid, and height information is obtained in addition to the lateral dimensions of the particles. These measurements of the particle size can help to reconcile the difference in particle size measured using neutron scattering and DLS.

5.2.3 Further Neutron Scattering Experiments

The present study has shown that the aqueous dispersions of phytoglycogen approach the jamming condition at the highest concentration measured (24.4 % w/w). It would be very interesting to perform SANS and QENS measurements on more concentrated dispersions to observe the effects of jamming in the neutron scattering data, e.g. decrease in particle size and change in water dynamics with jamming.

References

1. Powell, P. O. *et al.* Acid Hydrolysis and Molecular Density of Phyloglycogen and Liver Glycogen Helps Understand the Bonding in Glycogen α (Composite) Particles. *PLoS One* **10**, e0121337 (2015).
2. Ioan, C. E., Aberle, T. & Burchard, W. Solution properties of glycogen. 1. Dilute solutions. *Macromolecules* **32**, 7444–7453 (1999).
3. Sullivan, M. a. *et al.* Molecular insights into glycogen ??-particle formation. *Biomacromolecules* **13**, 3805–3813 (2012).
4. Manners, D. J. Recent developments in our understanding of glycogen structure. *Carbohydr. Polym.* **16**, 37–82 (1991).
5. Meléndez, R., Meléndez-Hevia, E., Mas, F., Mach, J. & Cascante, M. Physical constraints in the synthesis of glycogen that influence its structural homogeneity: a two-dimensional approach. *Biophys. J.* **75**, 106–114 (1998).
6. Meléndez, R., Meléndez-Hevia, E. & Canela, E. I. The fractal structure of glycogen: A clever solution to optimize cell metabolism. *Biophys. J.* **77**, 1327–1332 (1999).
7. Morris, G. a. *et al.* Molar mass and solution conformation of branched $\alpha(1 \rightarrow 4)$, $\alpha(1 \rightarrow 6)$ Glucans. Part I: Glycogens in water. *Carbohydr. Polym.* **71**, 101–108 (2008).
8. Sullivan, M. a *et al.* Nature of alpha and beta particles in glycogen using molecular size distributions. *Biomacromolecules* **11**, 1094–1100 (2010).
9. Putaux, J. L., Potocki-Véronèse, G., Remaud-Simeon, M. & Buleon, A. α -D-glucan-based dendritic nanoparticles prepared by in vitro enzymatic chain extension of glycogen. *Biomacromolecules* **7**, 1720–1728 (2006).
10. Takata, H., Kajiura, H., Furuyashiki, T., Kakutani, R. & Kuriki, T. Fine structural properties of natural and synthetic glycogens. *Carbohydr. Res.* **344**, 654–659 (2009).
11. Kajiura, H., Takata, H., Kuriki, T. & Kitamura, S. Structure and solution properties of enzymatically synthesized glycogen. *Carbohydr. Res.* **345**, 817–824 (2010).
12. Meléndez, R., Meléndez-Hevia, E. & Cascante, M. How did glycogen structure evolve to satisfy the requirement for rapid mobilization of glucose? A problem of physical constraints in structure building. *J. Mol. Evol.* **45**, 446–455 (1997).

13. Scheffler, S. L., Huang, L., Bi, L. & Yao, Y. In vitro digestibility and emulsification properties of phytoglycogen octenyl succinate. *J. Agric. Food Chem.* **58**, 5140–5146 (2010).
14. Highly monodisperse phytoglycogen particles act as hard sphere dispersions in water. Unpublished Manuscript.
15. ATR-IR Studies of Water Structure in Phytoglycogen and Hyaluronic Acid Films. Unpublished Manuscript.
16. Putaux, J., Bule, A., Borsali, R. & Chanzy, H. Ultrastructural aspects of phytoglycogen from cryo-transmission electron microscopy and quasi-elastic light scattering data. **26**, 145–150 (1999).
17. Garamus, V. M. *et al.* Hyperbranched polymers: Structure of hyperbranched polyglycerol and amphiphilic poly(glycerol ester)s in dilute aqueous and nonaqueous solution. *Macromolecules* **37**, 8394–8399 (2004).
18. Ballauff, M. & Likos, C. N. Dendrimers in solution: Insight from theory and simulation. *Angew. Chemie - Int. Ed.* **43**, 2998–3020 (2004).
19. Boris, D. & Michael, R. A Self-Consistent Mean Field Model of a Starburst Dendrimer : Dense Core vs Dense Shell. *Macromolecules* **29**, 7251–7260 (1996).
20. Gennes, P. G. De, Hervet, H., Gennes, P. G. De, Statistics, H. H. & Lettres, D. P. Statistics of "starburst" polymers. **44**, 351–360 (1983).
21. Lescanec, R. L. & Muthukumar, M. Configurational characteristics and scaling behavior of starburst molecules: a computational study. *Macromolecules* **23**, 2280–2288 (1990).
22. Mansfield, M. L. Surface adsorption of model dendrimers. *Polymer (Guildf)*. **37**, 3835–3841 (1996).
23. Zook, T. C. & Pickett, G. T. Hollow-core dendrimers revisited. *Phys. Rev. Lett.* **90**, 015502 (2003).
24. Pötschke, D. Ballauff, M. Structure of dendrimers in solution as probed by scattering experiments. 157–187 (2002).
25. Pötschke, D., Ballauff, M., Lindner, P., Fischer, M. & Vögtle, F. Analysis of the structure of dendrimers in solution by small-angle neutron scattering including contrast variation. *Macromolecules* **32**, 4079–4087 (1999).
26. Maiti, P. K., Çağın, T., Wang, G. & Goddard, W. a. Structure of PAMAM dendrimers: Generations 1 through 11. *Macromolecules* **37**, 6236–6254 (2004).

27. Götze, I. O. & Likos, C. N. Conformations of Flexible Dendrimers: A Simulation Study. *Macromolecules* **36**, 8189–8197 (2003).
28. Sears, V. F. Neutron scattering lengths and cross sections. *Neutron News* **3**, 26–37 (1992).
29. Pynn, R. Neutron Scattering - A Primer. (1990).
30. Grillo, I. Scattering and Condensed Matter. *Soft-Matter Charact.* (2008).
31. Hammouda, B. Probing Nanoscale Structures—the Sans Toolbox. *NIST Cent. Neutron Res.* 224 (2010). doi:10.1016/j.nano.2007.10.035
32. Pynn, R. The Mathematical Foundations of Neutron Scattering. *Neutron Scatt. Prim.* 28–31 (1990).
33. Lopez-Rubio, A. & Gilbert, E. P. Neutron scattering: a natural tool for food science and technology research. *Trends Food Sci. Technol.* **20**, 576–586 (2009).
34. Guinier, A. & Fournet, G. *Small-Angle Scattering of X-rays*. (John Wiley and Sons, New York, 1955).
35. Glatter, O. & Kratky, O. *Small-Angle X-Ray Scattering*. (Academic Press, 1982).
36. Guinier, A. *X-Ray Diffraction: In Crystals, Imperfect Crystals, and Amorphous Bodies*. (W.H. Freeman and Co, 1963).
37. Götze, I. O. & Likos, C. N. Microscopic and coarse-grained correlation functions in concentrated dendrimer solutions. (2004). doi:10.1088/0953-8984/17/20/008
38. Percus, J. K. & Yevick, G. J. Analysis of Classical Statistical Mechanics by Means of Collective Coordinates. *Phys. Rev.* **110**, 1–13 (1958).
39. Pedersen, J. S. Determination of size distribution from small-angle scattering data for systems with effective hard-sphere interactions. *J. Appl. Crystallogr.* **27**, 595–608 (1994).
40. Kotlarchyk, M. & Chen, S. H. Analysis of small angle neutron scattering spectra from polydisperse interacting colloids. *J. Chem. Phys.* **79**, 2461 (1983).
41. Strey, T. 2 . Shapes (Scattering Intensity Models). (2006).
42. Abade, G. C., Cichocki, B., Ekiel-Jezewska, M. L., Nägele, G. & Wajnryb, E. Rotational and translational self-diffusion in concentrated suspensions of permeable particles. *J. Chem. Phys.* **134**, (2011).
43. Heidemann, A. & Alefeld, B. *Review of the Applications of Backscattering Techniques in Neutron Scattering and X-Ray Scattering*. (1992).

44. Pall Corporation. Ultrafiltration Fundamentals. **50**, 3–6
45. Bradford, M. M. A rapid and sensitive method for the quantitation of microgram quantities of protein utilizing the principle of protein-dye binding. *Anal. Biochem.* **72**, 248–254 (1976).
46. Bio Rad. Quick Start Bradford Instruction Manual. 1–35 (2014).
47. Berne, B. J. & Pecora, R. *Dynamic Light Scattering: With Applications to Chemistry, Biology, and Physics*. (Courier Corporation, 2000).
48. Sutherland, W. A Dynamical Theory of Diffusion for Non-Electrolytes and the Molecular Mass of Albumin. *Philos. J. Sci.* **9**, 781–785 (1905).
49. Zhao, J. K., Gao, C. Y. & Liu, D. The extended Q-range small-angle neutron scattering diffractometer at the SNS. *J. Appl. Crystallogr.* **43**, 1068–1077 (2010).
50. Arnold, O. *et al.* Mantid - Data analysis and visualization package for neutron scattering and μ SR experiments. *Nucl. Instruments Methods Phys. Res. Sect. A Accel. Spectrometers, Detect. Assoc. Equip.* **764**, 156–166 (2014).
51. SasView for Small Angle Scattering Analysis, See: <http://sasview.org/>.
52. Mamontov, E. & Herwig, K. W. A time-of-flight backscattering spectrometer at the Spallation Neutron Source, BASIS. *Rev. Sci. Instrum.* **82**, 085109 (2011).
53. Ehlers, G., Podlesnyak, a. a., Niedziela, J. L., Iverson, E. B. & Sokol, P. E. The new cold neutron chopper spectrometer at the Spallation Neutron Source: Design and performance. *Rev. Sci. Instrum.* **82**, (2011).
54. Azuah, R. T. *et al.* DAVE: A Comprehensive Software Suite for the Reduction, Visualization, and Analysis of Low Energy Neutron Spectroscopic Data. *J. Res. Natl. Inst. Stand. Technol.* **114**, 341 (2009).
55. Ioan, C. E., Aberle, T. & Burchard, W. Solution properties of glycogen. 2. Semidilute solutions. *Macromolecules* **32**, 8655–8662 (1999).
56. Brewster, R., Pincus, P. a. & Safran, S. a. Hybrid lipids as a biological surface-active component. *Biophys. J.* **97**, 1087–1094 (2009).
57. Huang, L. & Yao, Y. Particulate structure of phytoglycogen nanoparticles probed using amyloglucosidase. *Carbohydr. Polym.* **83**, 1665–1671 (2011).
58. Yun, S. H. & Matheson, N. K. Structures of the amylopectins of waxy, normal, amylose-extender, and wx:ae genotypes and of the phytoglycogen of maize. *Carbohydr. Res.* **243**, 307–321 (1993).

59. Liu, A. J. & Nagel, S. R. Nonlinear dynamics: Jamming is not just cool any more. *Nature* **396**, 21–22 (1998).
60. Trappe, V., Prasad, V., Cipelletti, L., Segre, P. N. & Weitz, D. a. Jamming phase diagram for attractive particles. *Nature* **411**, 772–775 (2001).
61. Perticaroli, S., Nakanishi, M., Pashkovski, E. & Sokolov, A. P. Dynamics of hydration water in sugars and peptides solutions. *J. Phys. Chem. B* **117**, 7729–7736 (2013).
62. Vineyard, G. H. Scattering of slow neutrons by a liquid. *Phys. Rev.* **110**, 999–1010 (1958).
63. Nickels, J. D. *et al.* Dynamics of protein and its hydration water: neutron scattering studies on fully deuterated GFP. *Biophys. J.* **103**, 1566–75 (2012).
64. Santucci, S. C., Fioretto, D., Comez, L., Gessini, a. & Masciovecchio, C. Is there any fast sound in water? *Phys. Rev. Lett.* **97**, 1–4 (2006).
65. Taschin, a, Bartolini, P., Eramo, R., Righini, R. & Torre, R. Evidence of two distinct local structures of water from ambient to supercooled conditions. *Nat. Commun.* **4**, 2401 (2013).
66. Zanotti, J.-M., Bellissent-Funel, M.-C. & Chen, S.-H. Relaxational dynamics of supercooled water in porous glass. *Phys. Rev. E* **59**, 3084–3093 (1999).
67. Lupi, L. *et al.* Hydration and aggregation in mono- and disaccharide aqueous solutions by gigahertz-to-terahertz light scattering and molecular dynamics simulations. *J. Phys. Chem. B* **116**, 14760–14767 (2012).
68. Perticaroli, S. *et al.* Broadband depolarized light scattering study of diluted protein aqueous solutions. *J. Phys. Chem. B* **114**, 8262–8269 (2010).
69. Bellissent-Funel, M.-C., Teixeira, J., Bradley, K. F. & Chen, S. H. Dynamics of hydration water in protein. *J. Phys. I* **2**, 995–1001 (1992).
70. Paolantoni, M. *et al.* Light scattering spectra of water in trehalose aqueous solutions: Evidence for two different solvent relaxation processes. *J. Phys. Chem. B* **113**, 7874–7878 (2009).
71. Suzuki, T. & Sota, T. Improving ab initio infrared spectra of glucose-water complexes by considering explicit intermolecular hydrogen bonds. *J. Chem. Phys.* **119**, 10133–10137 (2003).
72. Halle, B. Protein hydration dynamics in solution: a critical survey. *Philos. Trans. R. Soc. Lond. B. Biol. Sci.* **359**, 1207–1223; discussion 1223–1224, 1323–1328 (2004).

73. Denisov, V. P. & Halle, B. Protein hydration dynamics in aqueous solution. *Faraday Discuss.* 227–244 (1996). doi:10.1039/fd9960300227